



MODELING A THIN-FILM TRANSISTOR (TFT)

İBRAHİM BOZKURT

JANUARY, 2015

MODELING A THIN FILM TRANSISTOR (TFT)

**A THESIS SUBMITTED TO
THE GRADUATE SCHOOL OF NATURAL AND APPLIED SCIENCES OF
CANKAYA UNIVERSITY**

BY

İBRAHİM BOZKURT

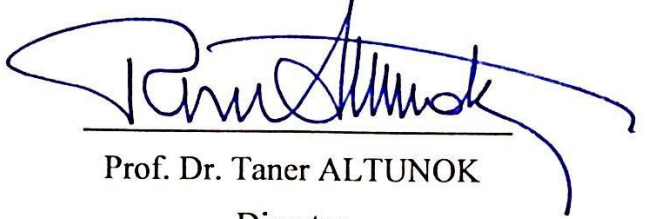
**IN PARTIAL FULLFILLMENT OF THE REQUIREMENTS
FOR
THE DEGREE OF MASTER OF SCIENCE
IN
THE DEPARTMENT OF
ELECTRONICS AND COMMUNICATION ENGINEERING**

JANUARY, 2015

Title of the Thesis : **Modeling a Thin Film Transistor (TFT)**


Submitted by **İbrahim BOZKURT**

Approval of the Graduate School of Natural and Applied Sciences, Çankaya University




Prof. Dr. Taner ALTUNOK
Director

I certify that this thesis satisfies all the requirements as a thesis for the degree of Master of Science.



Prof. Dr. Halil T. EYYÜBOĞLU
Head of Department

This is to certify that we have read this thesis and that in our opinion it is fully adequate, in scope and quality, as a thesis for the degree of Master of Science.



Prof. Dr. Celal Zaim ÇİL
Supervisor

Examination Date : 15.01.2015

Examination Committee Members:

Prof. Dr. Süleyman ÖZÇELİK (Gazi Univ.)

Prof. Dr. Celal Zaim ÇİL (Çankaya Univ.)

Assoc. Prof. Dr. Orhan GAZİ (Çankaya Univ.)



STATEMENT OF NON-PLAGIARISM PAGE

I hereby declare that all information in this document has been obtained and presented in accordance with academic rules and ethical conduct. I also declare that, as required by these rules and conduct, I have fully cited and referenced all material and results that are not original to this work.

Name, Last Name: İbrahim, BOZKURT

Signature :



Date :

15.01.2025

ABSTRACT

MODELING A THIN FILM TRANSISTOR (TFT)

BOZKURT, İbrahim

M.Sc., Department of Electronics and Communication Engineering

Supervisor: Prof. Dr. Celal Zaim ÇİL

January 2015, 63 Pages

In this thesis, we studied the working principles and modeling the static current – voltage characteristics of a Thin Film Transistor (TFT). TFTs are extensively used in flat panel displays for switching the pixels. We first analyzed the characteristics of Amorphous Indium Gallium Zinc Oxide (a-IGZO) TFTs, and reviewed the analytic models to estimate the static electrical behavior of the TFTs in general and the a-IGZO TFT, in particular. We developed a new analytical model for predicting the static electrical behavior of the a-IGZO TFTs and for analyzing and simulating the new electrical circuits when these transistors are used to form new circuits. Finally, we compared the predictions of this model with the measured data and other models.

Keywords: Semiconductor, TFT Models, IGZO, TFT Output Characteristics

ÖZ

İNCE FİLM TRANSİSTOR MODELLEME

BOZKURT, İbrahim

Yüksek Lisans, Elektronik ve Haberleşme Mühendisliği Anabilim Dalı

Tez Yöneticisi: Prof. Dr. Celal Zaim ÇİL

Ocak 2015, 63 Sayfa

Bu tez çalışmasında, ince film transistorların (TFT) çalışma prensipleri ve statik akım – gerilim karakteristiklerini çalıştık. TFT'lar yoğunlukla düz panel göstergelerinde görüntü gözelerini (piksel) sürmekte kullanılmaktadır. Öncelikle Amorf İndiyum Galyum Çinko Oksit (a-IGZO) TFT'lerin özelliklerini analiz ettik. Daha sonra genel olarak TFT'lerin özel olarak da a-IGZO TFT'lerin statik akım – gerilim davranışlarını kestirebilmek için geliştirilen analitik modelleri inceledik. a-IGZO TFT'lerin statik elektriksel davranışlarını kestirmek ve bunlar yeni devrelerde kullanıldığında, bu devrenin davranışını analiz ve simüle edebilmek amacıyla yeni bir analitik model geliştirdik. Bu modelin tahminlerini ölçülen değerler ve diğer modeller ile kıyasladık.

Anahtar Kelimeler: Yarıiletkenler, İnce Film Transistor Modelleri, IGZO, TFT Çıktı Özellikleri

ACKNOWLEDGEMENTS

I would like to express my deepest gratitude to my supervisor Prof. Dr. Celal Zaim ÇİL for his guidance and encouragement during my thesis study. I am very grateful for his leading role, advices and insight throughout the research.

I also wish to thank to all my family for their support and encouragement during my studies.

TABLE OF CONTENTS

STATEMENT OF NON-PLAGIARISM	iii
ABSTRACT	iv
ÖZ	v
ACKNOWLEDGEMENTS	vi
TABLE OF CONTENTS	vii
LIST OF FIGURES	viii
LIST OF TABLES	x
LIST OF ABBREVIATIONS	xi
CHAPTERS:	
1. INTRODUCTION	1
1.1. Why a-IGZO ?	6
2. ANALYTICAL TFT MODELS	12
2.1. The Analytical FET Models	14
3. NEW SURFACE POTENTIAL-BASED ANALYTIC IGZO TFT MODEL	36
3.1. Developing Our Model for an a-IGZO TFT	43
3.2. Fitting Theoretical Parts with Experimental Values	50
4. CONCLUSION	59
4.1. Conclusion	59
4.2. Future Work Plan	63
REFERENCES	R1
APPENDICES A	A1
SAMPLE MATLAB CODES	A1
APPENDICES B	A4
CURRICULUM VITAE	A4

LIST OF FIGURES

FIGURES

Figure 1	Some different types of basic TFT constructions [4].....	4
Figure 2	(a) Switching characteristics of an a-Si:H TFT (W=39 μ m, L=5 μ m)[3] (b) of a MOSFET[5].....	7
Figure 3	(a) input and (b) output characteristics of a-Si:H TFT [3].....	13
Figure 4	Cross sectional view of an n-channel FET [5].....	15
Figure 5	Gradual Channel Approximation of FET [5].....	17
Figure 6	Field effect mobility extracted from channel conductance in the linear region [3].....	18
Figure 7	(a) A cross-sectional schematic of a-IGZO TFT. (b) Energy-band diagram with definitions of $\Phi(x)$, Φ_{CH} and Φ_{FO} for the a-IGZO TFT [17].....	19
Figure 8	Φ_{SS} and Φ_{SD} calculation process	30
Figure 9	Φ_{SD} , V_{GS} and V_{DS} relation	30
Figure 10	Drain to source current curves in sub-threshold region for the TFT having the parameters listed in Table 2.1 (lines are used for guiding eyes only).....	32
Figure 11	Drain to source current curves in above-threshold region for the TFT having the parameters listed in Table 2.1 (lines are used for guiding eyes only).....	32
Figure 12	Total drain to source current curves (both sub and above threshold regions) for the TFT having the parameters listed in Table 2.1 (lines are used for guiding eyes only).....	33

FIGURES

	Changes in the characteristics for a 5% change in N_{EFF2}	
Figure 13	(curves in black color are the original curves, and the other curves for various colors are for decreased N_{EFF2} value).....	35
	Changes in the characteristics for a 5% change in kT_{EFF2}	
Figure 14	(curves in black color are the original curves, and the other curves for various colors are for decreased kT_{EFF2} value).....	35
Figure 15	Incremental field effect mobility (μ_{inc}) of an a-IGZO TFT [21]	41
Figure 16	I_{DS} curves by using Eq. 2.47.....	49
Figure 17	I_{DS} curves by using Eq. 3.20.....	50
	$I_{DS} - V_{DS}$ graphics (output characteristics) of an a-IGZO TFT	
Figure 18	from [18] used to obtain the measured data values for our model verification.....	51
Figure 19	Experimental data and our model fitting by changing γ	53
Figure 20	Drain and Gate voltage and best fitting γ relation.....	54
Figure 21	Snapshot of the custom equation surface fitting process screen	55

LIST OF TABLES

TABLES

Table 1	Comparison of Different TFT Technologies.....	10
Table 2	Geometrical and Extracted Model Parameters.....	29
Table 3	Geometrical and Extracted Model Parameters.....	48
Table 4	The Measured Data Values Obtained from Fig. 18 by an Image Processing Method (all data values are for 4 significant digits)..	52

LIST OF ABBREVIATIONS

AMLCD	Active Matrix Liquid Crystal Display
AMOLED	Active Matrix Organic Light Emitting Diode
a-Si:H	Hydrogenated Amorphous Silicon
a-IGZO	Amorphous Indium Gallium Zinc Oxide
CdSe	Cadmium Selenide
DOS	Density of States
FET	Field Effect Transistor
E_{IGZO}	Transverse Electric Field of IGZO TFT
kT_{EFF}	Characteristic Energy of Activation
LCD	Liquid Crystal Display
LTPS	Low Temperature Polycrystalline Silicon
MOSFET	Metal Oxide Semiconductor Field Effect Transistor
N_{EFF}	Effective Density of States (DOS)
n_{EFF}	Effective Carrier Density
n_{FREE}	Free Carrier Density
n_{LOC}	Localized Charge Density
TFT	Thin Film Transistor
ZnO	Zinc Oxide
Φ_s	Surface Potential
$\Phi(x)$	Transverse Electrical Potential
Φ_{CH}	Fermi Potential Lowering by the Drain Bias

Φ_{FO}	Fermi Potential Under Thermal Equilibrium
ϵ_{IGZO}	Permittivity of α -IGZO Active Layer
μ_{BAND}	Conduction Band Mobility
μ_{CH}	Channel (or Effective) Mobility

CHAPTER 1

1. INTRODUCTION

The image on a large LCD TV screen, or a small LCD mobile phone screen is produced by turning on some pixels and by turning off the others in accordance with the pattern determined by the image. The pixels are turned on by applying electrical current to the liquid crystal properly. The selected pixel generates the shade and not selected pixel passes the light with proper intensity and color. There are thousands of pixels on a display and all of them should be turned on, if needed, by applying electric currents to the selected pixels. This means every pixel on the display could be turned on or off by using a dedicated switch to that pixel. This switch is mostly a transistor operated non-linearly by driven either to ON state (driven into saturation), or to the OFF state (driven into cut-off) from a signal generated in accordance with the image to be displayed on the screen.

On a flat panel the transistors should be fabricated in a matrix array to switch the pixels. The most suitable type of transistor that would be for such an application is a metal-oxide semiconductor field-effect transistor (MOSFET), as it can be easily manufactured cost-effectively on a substrate planarly. Normally MOSFETs are produced on crystalline semiconductor substrate by either a p or n-type epitaxial growth of a crystalline semiconductor layer, and then two terminals at the two ends of a channel are produced by first doping these regions with proper atoms to make

them either p or n-type (opposite doping of the epitaxial region), and subsequently depositing metal regions on top of these doped regions. These metal terminals are called the drain (D) and the source (S). In between the drain and the source an oxide layer is formed and on top of this oxide layer a gate terminal is formed by using a proper conducting material. The channel formed between the source and the drain is turned on by applying a proper voltage to the gate and turned off by applying a voltage of the opposite polarity. This transistor, MOSFET, is the mostly used transistor type today in electronic devices, and the crystalline silicon (Si) is the most mature material to fabricate the very small size MOSFETs, making today the very large scale integrated circuits (VLSI) possible, where nearly 2 billion transistors can be manufactured on a semiconductor die of area of for example of 1mm^2 [1].

However, this type of MOSFETs are not proper to be used as a switch to turn on and off the pixels on a relatively large flat panel display, since firstly on flat displays we do not need the high density of transistors like we do in VLSI circuits, secondly these transistors are not to be produced on a semiconductor die of a very small size (such as $1\text{mm} \times 1\text{mm}$) but on a much larger flat glass displays (such as from $2\text{cm} \times 2\text{cm}$ to $2\text{m} \times 2\text{m}$). In a display we have generally a large glass panel and whatever to be deposited should be deposited on this panel of glass.

Therefore, on one hand to switch the pixels on the large displays it is sufficient to use relatively larger MOSFETS than those of on a crystalline silicon substrate, where one has to squeeze all the transistors in a very small area to make a very large scale integrated circuit chip (VLSIC). On the other hand, these bigger MOSFETs used to drive the pixels on the displays should also be manufactured with a cost effective way, on relatively large glass type materials. The most suitable technology to

manufacture such planar devices on large screens is the thin film deposition technology. A large glass screen can be put into a vacuum system, and a semiconductor, or metal or an organic material can be coated on it by using the thin film technology. The thin film is a film of thickness up to 1-2 micrometer. The vacuum system is made such that the thickness and the purity of the thin film can be controlled to a certain level of precision. When a semiconductor sheet is deposited on an amorphous material such as glass at relatively low temperatures ($\leq 400^{\circ}C$) the semiconductor thin film also becomes amorphous. However, after annealing the amorphous thin silicon films above $400^{\circ}C$, the material becomes polycrystalline. The annealing temperature should not exceed $500^{\circ}C$ when a glass substrate is used because glass cannot withstand these temperatures. Quartz can be used as a substrate to anneal the amorphous thin film semiconductor at higher temperatures to convert to crystalline semiconductor but quartz is not economical to be used on large displays.

As seen in Fig. 1, a thin film transistor (TFT) can be manufactured such that, an active layer that forms the channel is deposited first on a glass substrate. Two metal terminals for the source and the drain can be coated on the two ends of the channel by again metal deposition technique. Then an oxide layer is coated on the channel by chemical techniques. On top of the oxide between the two terminals another metal region can be formed as the gate [2].

In the TFT, as stated above, due to the glass substrates the channel layer formed cannot be made crystalline but it can be made mostly in amorphous or sometimes polycrystalline forms. To make p or n-type material from an amorphous or a polycrystalline material is very difficult but using some techniques such as sputtering

some amorphous semiconductors can be doped. Hydrogenated amorphous silicon (a-Si:H) is such a material that can be made slightly p or n-type. This is due to the passivation of the dangling bonds in the amorphous structure by the hydrogen atoms [3].

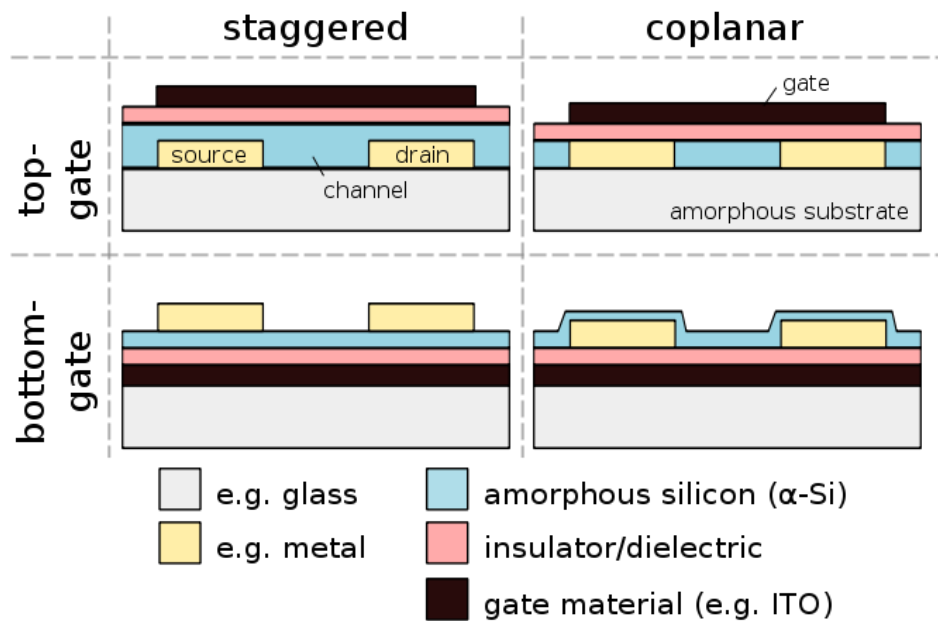


Figure 1 Some different types of basic TFT constructions [4]

In Fig. 1 we see some types of TFT configurations [4]. These are differing from each other in manufacturing order or physical properties. Thin film depositing technique is used to manufacture the devices in all these configurations.

a-Si:H TFTs are the first transistors that were used to switch the pixels on the flat displays. This type of TFT has hydrogenated amorphous silicon as channel material. Since a-Si:H is easily deposited on a substrate material such as glass by using mostly the sputtering technique under vacuum, it has been the first and mostly used material

to form a TFT [3]. Although they were widely used, a-Si:H TFTs have some disadvantages. Some of the disadvantages are low field - effect mobility, sensitivity to visible light, threshold voltage shift in off state, etc. These drawbacks are increasing the length between pixels and reducing some driving abilities of TFTs. a-Si:H TFTs were frequently used for AMLCDs backplanes, because high resolution is the most important parameter for AMLCDs, and an a-Si:H TFT can provide this. Drawbacks of a-Si:H TFTs show themselves in active-matrix organic light emitting diode (AMOLED) displays, hence they are not a good choice to drive AMOLEDs. AMOLED displays can be used not only for large flat panel application but also for flexible panel applications. This makes producing flexible electronic devices such as electronic papers, wearable technologies, etc. possible.

It is not easy and cost effective to run AMOLEDs with a-Si:H TFT driver circuit that can be used in AMLCDs [6-8]. So, researches have been investigating to find different materials to be used in the TFTs. Some examples for the alternative active channel material for the TFTs are low-temperature polycrystalline Si (LTPS) [9], pentacene-based organic materials [10], and metal-oxide semiconductors, which are mostly based on polycrystalline zinc oxide (ZnO) [11, 12] and amorphous metal oxide semiconductors [13].

The TFTs using pentacene-based organic materials in active layers were proven to be not reliable and stable. LTPS TFTs are used in some devices and they have relatively good performances. Especially, they provide good device performances with high field effect mobility values. However, they suffer from low level of uniformity when they were used on backplane of large panel areas [9,10].

Metal-oxide semiconductors show better performances than the above cited materials in these applications. They are able to be uniformly deposited on large backplane areas at low temperatures. They have higher mobility values, and are also not affected from visible light. These materials, when being mostly polycrystalline, have large grain boundaries at room temperature. This causes low performance at this temperature and decreases their stability on large backplane areas.

The recently introduced amorphous Indium Gallium Zinc Oxide Thin Film Transistors (a-IGZO TFTs) show much higher field effect mobilities than a-Si:H TFTs and do not suffer from grain boundaries as the polycrystalline materials do[14]. Backplanes that are produced by using that type of TFTs are used in both AMLCDs and AMOLEDs [15, 16].

1.1. Why a-IGZO ?

Although the TFTs are very suitable to be manufactured on large flat displays, regarding their switching performance they are rather much inferior to the MOSFETs made on crystalline semiconductors. The TFTs form the active switches in an active-matrix liquid crystal display (AMLCD), where the ON current determines the rate of pixel charging and the OFF current is associated with the leakage of the pixel voltage [3]. The switching characteristics of a MOSFET of a crystalline semiconductor and a TFT are shown in Fig. 2-a and -b, where the drain current is the current that flows between the drain and the source. As seen a MOSFET has much higher ON currents than the TFT, since in a MOSFET the mobility of carriers is much higher than a TFT.

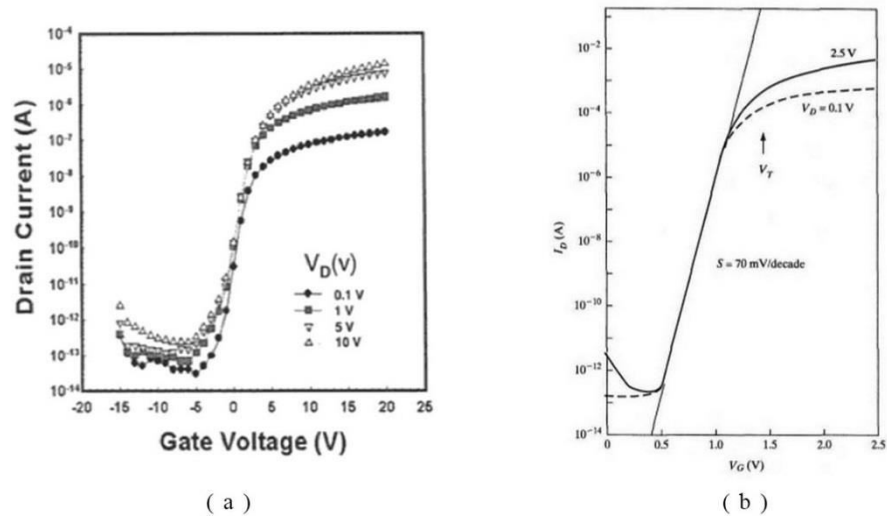


Figure 2 (a) Switching characteristics of an a-Si:H TFT ($W=39\mu\text{m}$, $L=5\mu\text{m}$)[3] (b) of a MOSFET[5]

In improving TFTs, efforts were increasingly focused on the issues of stability, ON/OFF Ratio, OFF current and leakage. The TFT, when switched, the ON/OFF currents ratio for proper LCD addressing applications should not be less than 10^6 . The OFF current should be less than 1nA. As described by Lee et al. [20] stability was always an important issue, the threshold voltage could change in years for example in the TFTs of *CdSe* active layers. TFTs have been notorious for their poor DC stability, which manifest itself as a slow decay of drain current when the device is operated with a steady gate voltage [3].

In 2010 the state-of-art Gen-8 facility is able to process glass substrate approximately 2160×246 mm in size, which produced up to six 52-inch flat panel TV screens from one single substrate [21]. The typical plasma enhanced chemical vapor deposition (PECVD) a-Si:H TFT has field effect mobility (μ_{EFF}) of $0.6-0.8$ cm^2/Vs , OFF-state drain current (I_{D_off}) below 10^{-13} A, and an ON-OFF ratio about 10^7 [22].

These properties are suitable for LCD switching but the μ_{EFF} would be insufficient for the new requirements of next generation displays, especially when the number of pixels are increasing (higher resolution) and more than 100 Hz of frame rate is needed on the TV screens to prevent the blurring effect [21].

The other issue in the active-matrix flat panel display (AM-FPD) is the emissive display such as active-matrix organic light emitting diode (OLED), where AMOLED is directly integrated with the TFT pixel electrode circuit. AMOLED does not need backlight as the AMLCD does, can have extremely high contrast ratio and delivers much better picture quality than AMLCD. However, AMOLED has more stringent requirements on the TFT backplane. Unlike LCD which only requires external electric field to change its phase, OLED takes significant amount of current to produce light by itself. The μ_{EFF} of a-Si:H TFT is not high enough to drive a large-area AMOLED. The TFT may constantly operate under high bias; a long term electrical instability is another concern and can also make the pixel electrode circuit design more complicated [21].

The application of a-Si:H TFT backplane is not limited to AMFPD. By integrating the photodiode or radiation sensitive layer with the backplane, a-Si:H TFT can also be used for sensor readout [21, 23]. One important example is the flat panel X-ray imager used for medical imaging [21, 24, 25, 26]. In order to achieve desirable signal gain on the active pixel sensor for signal readout TFTs used for both amplifying and readout TFTs should have a large width-over-length ratio (W/L) of about $150\mu m/25\mu m$ when using a-Si:H as the channel semiconductor material for the TFT. These transistors take the significant amount of the pixel area (about 50% of

250 μm^2 pixel size) resulting in a smaller resolution ($\leq 200\text{dpi}$) [21, 27, 28]. In a TFT if the mobility is lower than required, like a-Si:H TFT, one has to increase the W/L to increase the channel current, which causes a larger TFT area and reduces the resolution. Therefore, for a definite gate length (L) using a TFT having a larger mobility is one possible solution to achieve a smaller pixel area without sacrificing the gain performance. It is clear that a new high mobility semiconductor material yet with a uniform amorphous phase over a large area is highly desired [21].

Since 2004, there has been great interest in adapting TFT made of ionic amorphous oxide semiconductors [29]. Specifically, the ternary oxide system that consists of In_2O_3 , Ga_2O_3 and ZnO have shown promising electrical performance for TFT active layer with a high μ_{EFF} ($3-12 \text{ cm}^2/\text{Vs}$), low I_{D_off} ($\leq 10^{-12} \text{ A}$) and good uniformity compatible with the state-of-the-art Gen-8 substrate size [21, 30, 31].

Table 1 compares amorphous In-Ga-Zn-O (a-IGZO) with other TFT Technologies [21]. It is seen that a-IGZO is the only technology available today that can achieve a desired balance between high mobility and large area uniformity. Although polycrystalline (poly-Si) TFT is currently has the largest mobility it required additional re-crystallization steps such as excimer laser annealing [21, 32], metal seeding [33], or solid phase crystallization [34]. These add more complexity and cost to the process. Also the substrate area used by poly-Si TFT technology (Gen-4, 730x920 mm) is about 4 generations behind what a-Si:H TFT can achieve today (Gen-8) [21,35].

Technology	Mobility (cm ² /Vs)	Visible Light Transparency	Large Area Uniformity	Comments
a-Si:H	<1	Poor	Good (Gen-8)	Low mobility, limited current driving capability
Poly-Si	~100	Poor	Poor (Gen-4)	Additional crystallization process required
ZnO	20~50	Good	Poor	Strong tendency to form poly phase
a-IGZO	3~12	Good	Good (Gen-8)	Balance between mobility and uniformity

Table 1 Comparison of different TFT technologies [21]

Mono-oxide semiconductor, ZnO , has been used as the active layer in TFT channel. ZnO layer can be deposited by pulse laser deposition (PLD), RF magnetron sputtering or atomic layer deposition (ALD) and the ZnO TFT's μ_{EFF} is around $20-50 \text{ cm}^2 / Vs$. Despite this high mobility, due to its strong poly-crystalline nature even when deposited at room temperature the grain boundary of such oxide semiconductor affects device electrical properties, uniformity and stability over a large area [21,36,37,38]. For a TFT to have a low I_{D_off} and a high ON-OFF ratio, it is important to control the semiconductor carrier concentration to a very low level. In this sense a-IGZO is much better than ZnO or $CdSe$ [21, 39].

Even though a-Si:H is widely used in TFT backplane, it absorbs visible photons and has a low visible light transmittance ($\leq 30\%$). This has been a major drawback for utilizing such material in optoelectronics and can even raise concern of light-induced instability. On the other hand, similar to ZnO , a-IGZO has a wide bandgap ($\approx 3eV$)

and is highly transparent in visible light. This property opens up to new path of application such as transparent electronics or see-through display. In addition, light may directly transmit through a-IGZO TFT [21]. In conclusion, a-IGZO TFTs shows unique physical properties and better electrical performance over traditional a-Si:H TFTs, poly-Si TFTs and *ZnO* or *CdSe* TFTs.

A very thorough analysis of the amorphous oxide semiconductors (AZO) in general, IGZO TFTs in particular, is given by Kamiya et.al.[40]. They asserted that the a-IGZO TFTs would meet all the requirements for organic light emitting diode (OLED) displays, large and fast LCDs, 3-D displays, which cannot be satisfied by conventional silicon and organic TFTs. The reasons why the a-IGZO TFT will dominate this area in the future were listed by them [40], some of which are that most device issues, such as uniformity, long-term stability against bias stress and TFT performance are solved for a-IGZO TFTs, and 8G sputtering apparatus was developed and mature enough to manufacture these TFTs on large substrates.

We believed that the future switching device to drive the pixels on large displays would be a-IGZO TFT, and therefore, we studied modeling this transistor in this thesis.

In this thesis, we analyzed the IGZO TFT characteristics and analytic models developed for this type of TFTs. Then, we proposed and developed a new analytic model for an a-IGZO TFT.

CHAPTER 2

2. ANALYTICAL TFT MODELS

A transistor is a three-terminal semiconductor device. There are generally two classes of transistors: a bipolar junction transistor (BJT), and a field effect transistor (FET). A TFT is an FET type transistor. In an FET transistor a channel that carries the current is formed between the source and drain terminals. The channel's conductivity, and therefore the drain current (I_D) that flows through the channel, is controlled by the voltage applied at the gate terminal (V_{GS}). The static (direct current: DC) behavior of a transistor is sufficiently described by the input characteristics and the output characteristics. In the input characteristics of an FET, I_D versus V_{GS} is given for a fixed V_{DS} , where V_{DS} is the voltage applied between drain and the source. The output characteristics are between I_D and V_{DS} for constant values of V_{GS} as parameter. Fig. 3-a and -b are the examples for the input and the output characteristics, of an a-Si:H TFT, respectively.

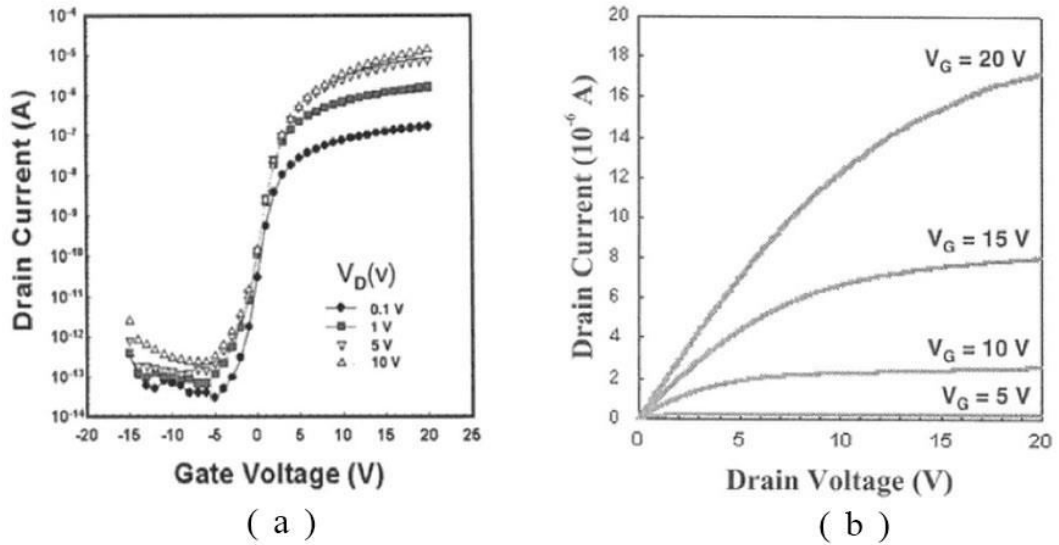


Figure 3 (a) input and (b) output characteristics of a-Si:H TFT [3]

Modeling a transistor is to obtain mathematical relations between I_D , V_{GS} and V_{DS} , by using the transistor's geometric properties and material characteristics to understand and improve the device electrical performance. The higher the conformance of the model predictions with the measured characteristics, the better the model. Models can be analytical and numerical. Analytical models are given by closed-form mathematical equations that can be solved analytically and easier to use generally. Analytical models can be easily used in computer-aided design (CAD) tools to simulate the circuit behavior as well. However, they are limited in deriving 2- and 3-dimensional device behavior and sometimes are not accurate enough. Numerical models can better represent the device physics [3] especially in 2-and 3-dimensions. These are mostly given by some partial differential equations, or integrals that can only be solved by numerical techniques for certain boundary and initial conditions. Numerical models could be more accurate than analytical models but generally they are more difficult and impractical to deal with. They mostly require relatively bigger computer resources and they take much longer times to run.

The model is used to predict the behavior of the device before manufacturing it, and at the same time they could be used to derive certain parameters using measured values subsequent to production of the device. The model is mostly used for designing the device to the desired performance. It serves also as a tool for analyzing the behavior of the device produced using the measured data.

In this thesis, we developed an analytical model for predicting and representing the DC behavior of an a-IGZO TFT. Before presenting our model, in this chapter we provide the simplest model first. This is the constant mobility model where a gradual channel formation between the drain and the source is assumed. Then, we analyzed in detail a variable channel mobility model, where the mobility is given by the carrier concentrations for an a-IGZO TFT [17].

2.1. The Analytical FET Models

2.1.1. The Gradual Channel Approximation FET Model

Fig. 4 shows an FET, where x denotes the direction from the gate terminal to the substrate, that is, the transverse direction, which is perpendicular to the channel; and y denotes the direction from the source terminal to the drain terminal, which is parallel to the channel.

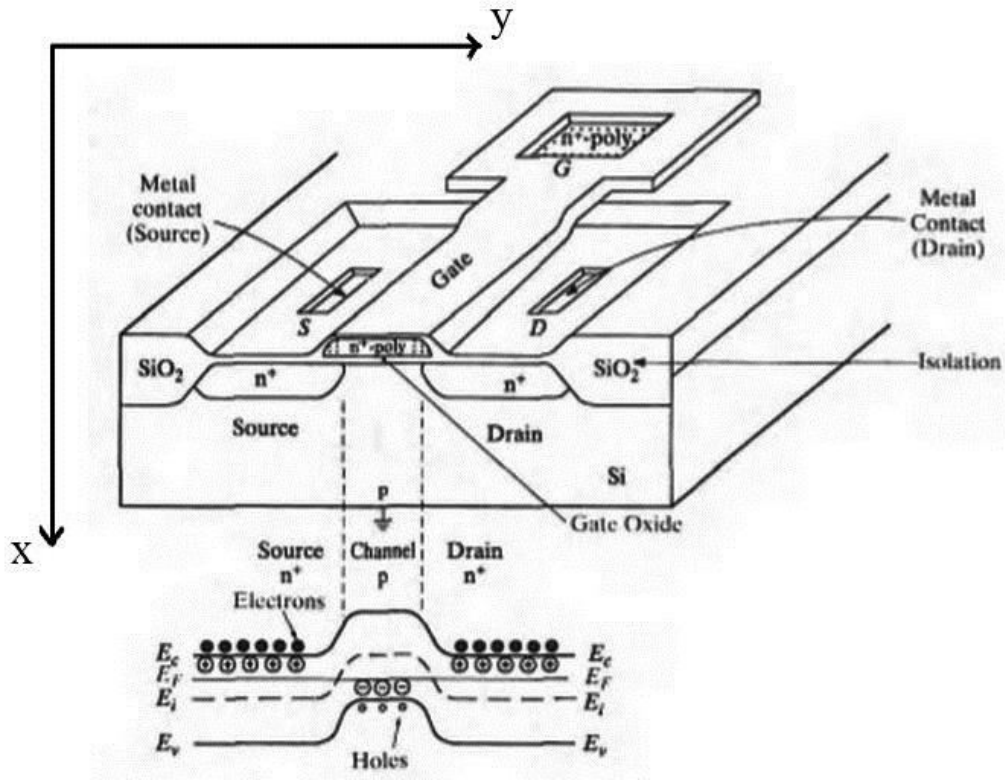


Figure 4 Cross sectional view of an n-channel FET [5]

A voltage applied to the gate changes the free charge concentration in the channel. Changing the number of free carriers per cross sectional area in the channel modulates the conductivity and hence the drain current.

If we assume a gradual channel is formed between drain and source under the influence of both V_{GS} and V_{DS} voltages, and a constant carrier mobility in the channel, when the gate potential is higher than the threshold voltage, V_{TH} , the mobile charge Q_I in the channel is related to the gate potential V_{GS} via [3]

$$Q_I = -C_{ox} [V_{GS} - V_{TH} - V(y)] \quad (2.1)$$

where C_{ox} is the capacitance per unit area of the SiN_x gate oxide, and $V(y)$ is the channel potential at a certain y value. The current induced by the majority carriers, in this case electrons for an n-channel FET, can be given as

$$I_D = W\mu_n Q_i E_y \quad , \quad (2.2)$$

where W is the channel width, μ_n is the electron mobility, and E_y is the electric field at y . By substituting $E_y = \frac{-dV(y)}{dy}$ into Eq. 2.2, we get;

$$I_D dy = W \mu_n C_{ox} [V_{GS} - V_{TH} - V(y)] dV(y) \quad (2.3)$$

By integrating the current along the channel (from $y=0$ to $y=L$, the channel length), using $V(0)=0$ at the source and $V(L)=V_{DS}$ at the drain, we obtain the drain current for the linear region;

$$I_D = \frac{C_{ox}\mu_n W}{L} [(V_{GS} - V_{TH})V_{DS} - 1/2 V_{DS}^2] \quad (2.4)$$

In this region where $V_{DS} \ll V_{GS}$;

$$I_D \cong \frac{C_{ox}\mu_n W}{L} (V_{GS} - V_{TH}) V_{DS} \quad (2.5)$$

As seen in Fig. 3-b, in the linear region where $(V_{DS} \ll V_{GS})$ holds, for a constant V_{GS} , the current changes linearly with V_{DS} .

The saturation region, where the current saturates and becomes nearly constant even the V_{DS} increases, is the point where the field-induced carrier density at the drain side disappears as the drain potential increases. Eventually, when

$$V_{DS} = V_{GS} - V_{TH} \quad (2.6)$$

the channel with induced electrons becomes completely depleted of the electrons where this condition is realized. This is called the pinch-off of the channel, where the drain current saturates. For $V_{DG} \geq V_{GS} - V_{TH}$ Eq. 2.4 and 2.5 are no longer valid. The saturation drain current can be obtained by substituting Eq. 2.6 into 2.5, giving [3]

$$I_D = \frac{C_{ox}\mu_n W}{2L} (V_{GS} - V_{TH})^2. \quad (2.7)$$

The model gives a fairly good fit to the curves in the linear region and also predicts the saturation point (pinch-off); however, it predicts that after this point the drain current is constant even V_{DS} continues to increase.

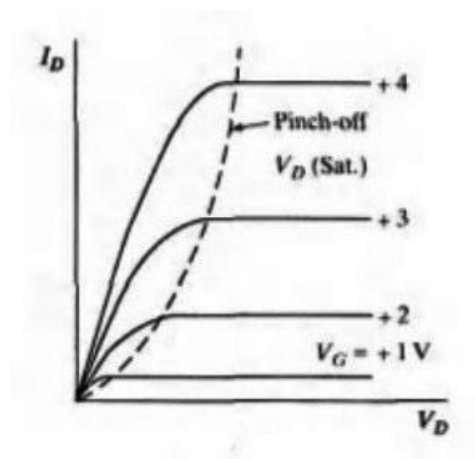


Figure 5 Gradual Channel Approximation of FET [5]

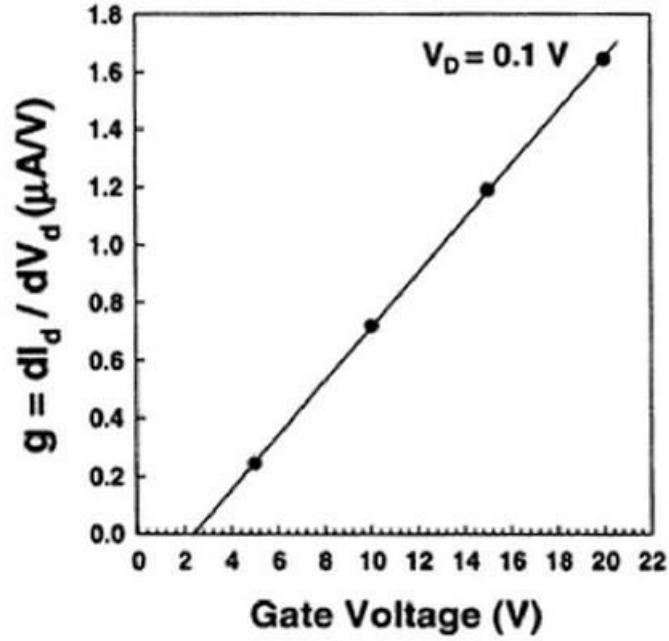


Figure 6 Field effect mobility extracted from channel conductance in the linear region [3]

One can determine the field-effect mobility, or the channel mobility (μ_n), from Fig. 6 by using Eq. 2.7. Deviations from the gradual channel approximation model are often related to contact resistance effects and gate-voltage dependent mobility [3]. The field-effect mobility of the electrons in the channel of an a-Si:H TFT is only related to the 10% of the extended-state conduction-band mobility because of multiple carrier trapping in the band tail states.

2.1.2. The model based on a mobility that changes with carrier concentrations in the channel for an a-IGZO TFT [17]

In this model, we provide a more accurate analytical model for an a-IGZO TFT. The geometry of the a-IGZO TFT is given in Fig. 3-a. In this model we do not assume a gradual channel. At any point in the channel the carrier concentration is dependent

on the potential $\Phi(x)$. The surface potential (Φ_s) is changed with V_{GS} and V_{DS} . Amorphous - Indium Gallium Zinc Oxide (a-IGZO) is the active channel material in this transistor. We derived all the equations step by step clearly. Effective electron density (n_{EFF}) is an important parameter in analytic DC model. In an n-type a-IGZO channel material, there are conduction band electrons (n_{FREE}) and the carriers that hop under effect of the potential in the localized deep states within the conduction band (n_{LOC}). Because n_{EFF} is the effective concentration of electrons that contributes the channel conductivity. It is composed of n_{FREE} and n_{LOC} .

$$n_{EFF}(x) = n_{FREE}(x) + n_{LOC}(x) \quad (2.8)$$

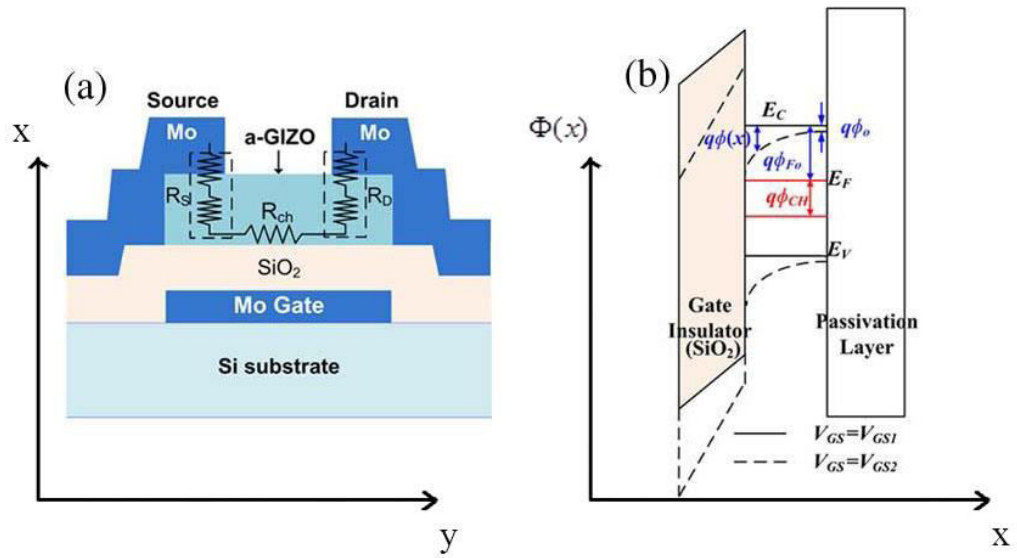


Figure 7 (a) A cross-sectional schematic of a-IGZO TFT. (b) Energy-band diagram with definitions of $\Phi(x)$, Φ_{CH} and Φ_{FO} for the a-IGZO TFT [17]

In Fig. 3-a, the cross-sectional schematic of a-IGZO TFT with channel resistance (R_{CH}) and parasitic resistances ($R_p(V_{GS}, V_{DS})$) is given. The energy – band diagram in Fig. 3 also shows how the potential changes in x direction ($\Phi(x)$), Fermi potential is lowered by the drain bias (Φ_{CH}) and Fermi potential under thermal equilibrium (Φ_{FO}). Poisson's equation is expressed for potential $\Phi(x)$ as

$$\frac{\partial^2 \Phi}{\partial x^2} = -\frac{\rho(x)}{\epsilon_{IGZO}} = \frac{qn_{EFF}(x)}{\epsilon_{IGZO}} \quad (2.9)$$

Eq. 2.9 defines the relation between charge density and potential. $\rho(x)$ is charge density and ϵ_{IGZO} is permittivity of the a-IGZO active layer. When Eq. 2.8 and Eq.2.9 are combined, we can easily understand there is a direct relationship between charge density and free carriers and localized charges. Eq. 2.10 shows that relation clearly.

$$\frac{\rho(x)}{q} = -(n_{FREE}(x) + n_{LOC}(x)) = -n_{EFF}(x) \quad (2.10)$$

$$E_{IGZO} = -\frac{d\Phi}{dx}, \quad (2.11)$$

where E_{IGZO} is the electric field generated by the applied voltage at x . Eq. 2.11 also gives important information about the relation of electric field with charge density.

Eq. 2.9 and Eq. 2.11 are combined by using the algebraic rule given by

$$\frac{\partial \left[\frac{\partial f(x)}{\partial x} \right]}{\partial x} = 2 \left[\frac{\partial f(x)}{\partial x} \right] \left[\frac{\partial^2 f(x)}{\partial x^2} \right]. \quad (2.12)$$

By using this in Eq. 2.12, Eq. 2.9 can be written by using Eq. 2.11 as

$$\frac{\partial \left[\frac{\partial \Phi}{\partial x} \right]^2}{\partial x} = 2 \left[\frac{\partial \Phi}{\partial x} \right] \left[\frac{\partial^2 \Phi}{\partial x^2} \right] \quad (2.13)$$

$$\frac{\partial}{\partial x} [-E_{IGZO}]^2 = 2 \left[\frac{\partial \Phi}{\partial x} \right] \left(-\frac{\rho(x)}{\epsilon_{IGZO}} \right). \quad (2.14)$$

Now, we are trying to find the electric field in terms of effective carrier density. We integrate both sides of Eq. 2.14.

$$\int \frac{\partial}{\partial x} [E_{IGZO}]^2 dx = -\frac{2}{\epsilon_{IGZO}} \int \rho(x) \frac{\partial \Phi}{\partial x} dx \quad (2.15)$$

$$E_{IGZO}^2(\Phi(x)) = \frac{2q}{\epsilon_{IGZO}} \int n_{EFF}(x) d\Phi(x) \quad (2.16)$$

$n_{EFF}(x)$ can be expressed in terms of potentials as

$$n_{EFF}(x) = N_{EFF} \exp \left[\frac{q(\Phi(x) - \Phi_{FO} - \Phi_{CH})}{kT_{EFF}} \right]. \quad (2.17)$$

In Eq. 2.17, N_{EFF} is the effective Density of States (DOS) in cm^{-3} and kT_{EFF} is characteristic slope in eVs. By combining Eq. 2.16 and Eq. 2.17, we can express the electric field in terms of potentials in Eq. 2.18.

$$E_{IGZO}^2(\Phi(x)) = \frac{2q}{\varepsilon_{IGZO}} \int N_{EFF} \exp\left[\frac{q(\Phi(x) - \Phi_{FO} - \Phi_{CH})}{kT_{EFF}}\right] d\Phi(x) \quad (2.18)$$

Finally, when we take the integral in Eq. 2.18, we find the electric field E_{IGZO} in terms of potentials.

$$E_{IGZO}^2(\Phi(x)) = \frac{N_{EFF}kT_{EFF}}{\varepsilon_{IGZO}} \exp\left[\frac{q(\Phi(x) - \Phi_{FO} - \Phi_{CH})}{kT_{EFF}}\right] \quad (2.19)$$

In next step, we derive the total charge by using the electric field that is given by Eq. 2.19 and total free charge. Total free charge is given in Eq. 2.20.

$$Q_{FREE}(\Phi(x)) = q \int_{x=0}^{x=T_{IGZO}} n_{FREE}(\Phi(x)) dx \quad (2.20)$$

$$n_{FREE}(\Phi(x)) = N_c \exp\left[\frac{q(\Phi(x) - \Phi_{FO} - V_{CH}(y))}{kT}\right] \quad (2.21)$$

After we have combined Eq. 2.20 and Eq. 2.21, we are ready to find the total charge.

In addition to that process, we combine Eq. 2.22 with Eq. 2.19.

$$Q_{FREE}(\Phi(x)) = qN_c \int_{x=0}^{x=T_{IGZO}} \exp\left[\frac{q(\Phi(x) - \Phi_{FO} - V_{CH}(y))}{kT}\right] dx \quad (2.22)$$

In Eq. 2.19 square of E_{IGZO} is given and electric field is also the negative derivative of $\Phi(x)$ as it is written in Eq. 2.11. By using this equation, Eq. 2.23 is developed.

$$-\frac{d\Phi(x)}{dx} = \sqrt{\frac{2N_{EFF}kT_{EFF}}{\varepsilon_{IGZO}}} \exp\left[\frac{q(\Phi(x) - \Phi_{FO} - V_{CH})}{2kT_{EFF}}\right] \quad (2.23)$$

Now, we obtain dx by using Eq. 2.23 to use that information in Eq. 2.22.

$$dx = -\frac{1}{\sqrt{\frac{2N_{EFF}kT_{EFF}}{\epsilon_{IGZO}}}} \exp\left[\frac{-q(\Phi(x) - \Phi_{FO} - V_{CH})}{2kT_{EFF}}\right] d\Phi(x) \quad (2.24)$$

$$\begin{aligned} Q_{FREE}(\Phi(x)) &= qN_c \int_0^{\Phi(x)} \exp\left[\frac{q(\Phi(x) - \Phi_{FO} - V_{CH}(y))}{kT}\right] \\ &\times \left(\sqrt{\frac{\epsilon_{IGZO}}{2N_{EFF}kT_{EFF}}} \exp\left[\frac{-q(\Phi(x) - \Phi_{FO} - V_{CH})}{2kT_{EFF}}\right] \right) d\Phi(x) \end{aligned} \quad (2.25)$$

When we take the integral in Eq. 2.25;

$$\begin{aligned} Q_{FREE}(\Phi(x)) &= \frac{qN_c \sqrt{\epsilon_{IGZO}}}{\sqrt{2N_{EFF}kT_{EFF}} \left[\frac{1}{kT} - \frac{1}{kT_{EFF}} \right] q} \\ &\times \left(\exp\left[\left(\frac{1}{kT} - \frac{1}{kT_{EFF}} \right) (q(\Phi(x) - V_{CH} - \Phi_{FO})) \right] \right) \end{aligned} \quad (2.26)$$

We use the parameters in Eq. 2.27 to simplify the equation.

$$A^* = \frac{N_c \sqrt{\epsilon_{IGZO}}}{B^* \sqrt{2N_{EFF}kT_{EFF}}} \quad B^* = \left(\frac{1}{kT} - \frac{1}{2kT_{EFF}} \right) \quad (2.27)$$

$$Q_{FREE}(\Phi(x)) = A^* \exp[qB^*(\Phi(x) - V_{CH}(y) - \Phi_{FO})] \quad (2.28)$$

The short representation of free charge is given in Eq. 2.28. Total charge is the sum of free and localized charges. At the same time, it equals the product of permittivity and electric field as shown in Eq. 2.29 and Eq. 2.30.

$$Q_{TOT}(\Phi(x)) = Q_{FREE}(\Phi(x)) + Q_{LOC}(\Phi(x)) = \epsilon_{IGZO} E_{IGZO}(\Phi(x)) \quad (2.29)$$

$$Q_{TOT}(\Phi(x)) = \sqrt{2\varepsilon_{IGZO}N_{EFF}kT_{EFF}} \exp\left[\frac{q(\Phi(x) - V_{CH}(y) - \Phi_{FO})}{2kT_{EFF}}\right] \quad (2.30)$$

By using Eq. 2.28 and Eq. 2.30 in Eq. 2.31, V_{GS} dependent channel mobility (μ_{CH}) can be found.

$$\mu_{CH}(\Phi(x)) = \mu_{BAND} \frac{Q_{FREE}(\Phi(x))}{Q_{FREE}(\Phi(x)) + Q_{LOC}(\Phi(x))} \quad (2.31)$$

μ_{BAND} is the conduction band mobility in Eq. 2.31. We insert the values given in Eq. 2.28 and Eq. 2.30 into Eq. 2.31

$$\mu_{CH}(\Phi(x)) = \mu_{BAND} \frac{A^* \exp[qB^*(\Phi(x) - V_{CH}(y) - \Phi_{FO})]}{\sqrt{2\varepsilon_{IGZO}N_{EFF}kT_{EFF}} \exp\left[\frac{q(\Phi(x) - V_{CH}(y) - \Phi_{FO})}{2kT_{EFF}}\right]} \quad (2.32)$$

$$\mu_{CH}(\Phi(x)) = \mu_{BAND} \frac{N_c}{\left(\frac{1}{kT} - \frac{1}{2kT_{EFF}}\right)(2N_{EFF}kT_{EFF})} \times \exp\left[\left(\frac{1}{kT} - \frac{1}{kT_{EFF}}\right)q(\Phi(x) - V_{CH}(y) - \Phi_{FO})\right] \quad (2.33)$$

Now, we describe drain to source current (I_{DS}) in terms of $\mu_{CH}(\Phi(x))$ and other terms in $\mu_{CH}(\Phi(x))$ equation. The drain to source current equation is

$$I_{DS} = W \frac{dV_{CH}}{dy} \int_{\Phi(x=T_{IGZO})}^{\Phi(x=0)} q\mu_{CH} \frac{n_{FREE}(\Phi(x))}{E_{IGZO}(\Phi(x))} d\Phi(x). \quad (2.34)$$

We take the integral in Eq. 2.34. μ_{CH} is given above in Eq. 2.33. $n_{FREE}(\Phi(x))$ can be written by using Eq. 2.21, and $E_{IGZO}(\Phi(x))$ can be found by using Eq. 2.19.

$$I_{DS} = W \frac{dV_{CH}}{dy} \int_{\Phi(x=T_{IGZO})}^{\Phi(x=0)} q\mu_{BAND} \frac{N_c}{(2N_{EFF}kT_{EFF})B^*} \frac{N_c\sqrt{\epsilon_{IGZO}}}{\sqrt{2N_{EFF}kT_{EFF}}} \times \exp\left[\left(\frac{1}{kT} + \frac{1}{kT} - \frac{1}{kT_{EFF}} - \frac{1}{2kT_{EFF}}\right)q(\Phi(x) - V_{CH}(y) - \Phi_{FO})\right] d\Phi(x) \quad (2.35)$$

To simplify, we use Eq. 2.27 and Eq. 2.36.

$$C^* = \left(\frac{2}{kT} - \frac{3}{2kT_{EFF}}\right) \quad (2.36)$$

$$I_{DS} = W \frac{dV_{CH}}{dy} q\mu_{BAND} \left(\frac{A^*N_c}{2N_{EFF}kT_{EFF}}\right) \times \int_{\Phi(x=T_{IGZO})}^{\Phi(x=0)} \exp[qC^*(\Phi(x) - V_{CH} - \Phi_{FO})] d\Phi(x) \quad (2.37)$$

If we take the integral we get

$$I_{DS} = W \mu_{BAND} \frac{dV_{CH}}{dy} \left(\frac{A^*N_c}{2N_{EFF}kT_{EFF}C^*}\right) \exp[qC^*(\Phi(x) - V_{CH} - \Phi_{FO})]. \quad (2.38)$$

In Eq. 2.38, we can clearly see that $\Phi(x=T_{IGZO}) = V_{CH} + \Phi_{FO}$ and $\Phi(x=0) = \Phi_S$.

We have found a near analytic DC I-V model. But, the surface potential (Φ_S) also depends on the Fermi level lowering effect along the channel [18]. So, we should find a relation between surface potential and the channel voltage (V_{CH}). At first, we

derive the relation between I_{DS} and V_{GS} and V_{DS} . We will apply Gauss Law to the boundary between a-IGZO active layer and the gate oxide. This operation gives us a nonlinear relation between V_{GS} and Φ_S

$$V_{GS} = V_{FB} + \Phi_S + \frac{\varepsilon_{IGZO} E_{IGZO}(\Phi_S, V_{CH})}{C_{OX}}. \quad (2.39)$$

Flat band voltage (V_{FB}) is of constant value, and surface potential (Φ_S) is variable.

Electric field can be found by using Eq. 2.19.

$$\frac{\varepsilon_{IGZO} E_{IGZO}(\Phi_S, V_{CH})}{C_{OX}} = \frac{\sqrt{2N_{EFF} kT_{EFF} \varepsilon_{IGZO}}}{C_{OX}} \exp\left(\frac{q(\Phi_S - V_{CH} - \Phi_{FO})}{2kT_{EFF}}\right) \quad (2.40)$$

By using Eq. 2.40, Eq. 2.39 can be expressed as

$$\frac{(V_{GS} - V_{FB} - \Phi_S) C_{OX}}{\sqrt{2\varepsilon_{IGZO} N_{EFF} kT_{EFF}}} = \exp\left(\frac{q(\Phi_S - V_{CH} - \Phi_{FO})}{2kT_{EFF}}\right) \quad (2.41)$$

Now, we express V_{CH} in terms of surface potential (Φ_S). The relation between V_{CH} and Φ_S is nonlinear

$$\Phi_S - V_{CH} - \Phi_{FO} = \frac{2kT_{EFF}}{q} \ln\left[\frac{C_{OX}(V_{GS} - V_{FB} - \Phi_S)}{\sqrt{2\varepsilon_{IGZO} N_{EFF} kT_{EFF}}}\right]. \quad (2.42)$$

Now, we take the derivative of channel voltage and use that equation in Eq. 2.38.

$$\frac{dV_{CH}(y)}{d\Phi_S(y)} = 1 + \frac{2kT_{EFF}}{q(V_{GS} - V_{FB} - \Phi_S)} \quad (2.43)$$

$$\frac{dV_{CH}(y)}{dy} = \frac{dV_{CH}(y)}{d\Phi_s(y)} \frac{d\Phi_s(y)}{dy} = \left[1 + \frac{2kT_{EFF}}{q(V_{GS} - V_{FB} - \Phi_s)} \right] \frac{d\Phi_s(y)}{dy} \quad (2.44)$$

When we put Eq. 2.42 and Eq. 2.44 into Eq. 2.38, we find a better expression for drain to source current. Eq. 2.45 is giving that equation.

$$I_{DS} = W \mu_{BAND} \left[1 + \frac{2kT_{EFF}}{q(V_{GS} - V_{FB} - \Phi_s)} \right] \frac{A^* N_c}{2N_{EFF} kT_{EFF} C^*} \times \left[\frac{C_{OX} (V_{GS} - V_{FB} - \Phi_s)}{\sqrt{2\varepsilon_{IGZO} N_{EFF} kT_{EFF}}} \right]^{2kT_{EFF} C^*} \frac{d\Phi_s(y)}{dy} \quad (2.45)$$

Finally, when we take the integral in y direction, the drain current is derived.

Integrating in y direction from 0 to L , $\Phi_{SS} = \Phi_s(y=0, V_{CH} = 0)$ and

$\Phi_{SD} = \Phi_s(y=L, V_{CH} = V_{DS})$ I_{DS} is obtained.

$$\int_{y=0}^{y=L} I_{DS} dy = \int_{\Phi_{SS}}^{\Phi_{SD}} W \mu_{BAND} \left[1 + \frac{2kT_{EFF}}{q(V_{GS} - V_{FB} - \Phi_s)} \right] \times \left(\frac{A^* N_c}{2N_{EFF} kT_{EFF} C^*} \left[\frac{C_{OX} (V_{GS} - V_{FB} - \Phi_s)}{\sqrt{2\varepsilon_{IGZO} N_{EFF} kT_{EFF}}} \right]^{2kT_{EFF} C^*} \right) d\Phi_s(y) \quad (2.46)$$

$$\begin{aligned}
I_{DS}(N_{EFF}, kT_{EFF}) &= \frac{W}{L} \mu_{BAND} \frac{A^* N_c}{2N_{EFF} kT_{EFF} C^*} \left(\frac{C_{OX}}{\sqrt{2\varepsilon_{IGZO} N_{EFF} kT_{EFF}}} \right)^{2kT_{EFF} C^*} \\
&\times \left\{ (2kT_{EFF} C^* + 1)^{-1} \right. \\
&\times \left((V_{GS} - V_{FB} - \Phi_{SS})^{2kT_{EFF} C^* + 1} - (V_{GS} - V_{FB} - \Phi_{SS})^{2kT_{EFF} C^* + 1} \right) \\
&\left. - (qC^*)^{-1} \times \left((V_{GS} - V_{FB} - \Phi_{SS})^{2kT_{EFF} C^*} - (V_{GS} - V_{FB} - \Phi_{SD})^{2kT_{EFF} C^*} \right) \right\}
\end{aligned} \tag{2.47}$$

Final version of the equation gives the relation among drain current, gate to source voltage and drain to source voltage. μ_{BAND} is an important parameter on which the drain current is directly proportional.

If there are two different parameters for sub and above of threshold region, the process is shown above should be done for these two regions. To find the total I_{DS} value, we will use

$$I_{DS_TOT} = \frac{1}{I_{DS_sub}(N_{EFF1}, kT_{EFF1})} + \frac{1}{I_{DS_above}(N_{EFF2}, kT_{EFF2})} \tag{2.48}$$

We have calculated all values of I_{DS_TOT} by using the formula given in Eq. 2.47.

There are many parameters in those equations. Those parameter values are given in [18].

Parameter	Value	Parameter	Value
W / L [μm]	225/30	N_{EFF1} [cm^{-3}]	8.7×10^{17}
L_{OV} [μm]	5	kT_{EFF1} [eV]	0.045
$T_{\text{OX}} / T_{\text{IGZO}}$ [nm]	100/50	N_{EFF2} [cm^{-3}]	5.15×10^{18}
μ_{BAND} [$\text{cm}^2 / \text{V.s}$]	19.7	kT_{EFF2} [eV]	0.0263
N_C [cm^{-3}]	4.8×10^{18}	C_{OX} [nF/ cm^2]	42.37
V_{FB} [V]	0.3	ϕ_{F0} [V]	0.3

Table 2 Geometrical and extracted model parameters [18]

By using those values given in Table 2.1, we obtained 3 similar figures. All these 3 figures given below show the relation between I_{DS} , V_{GS} , and V_{DS} . During that process, we have used Eq. 2.39 to calculate Φ_{SS} and Φ_{SD} values. The steps to obtain the individual values for I_{DS} by changing V_{GS} and V_{DS} values are given in the flow-chart below.

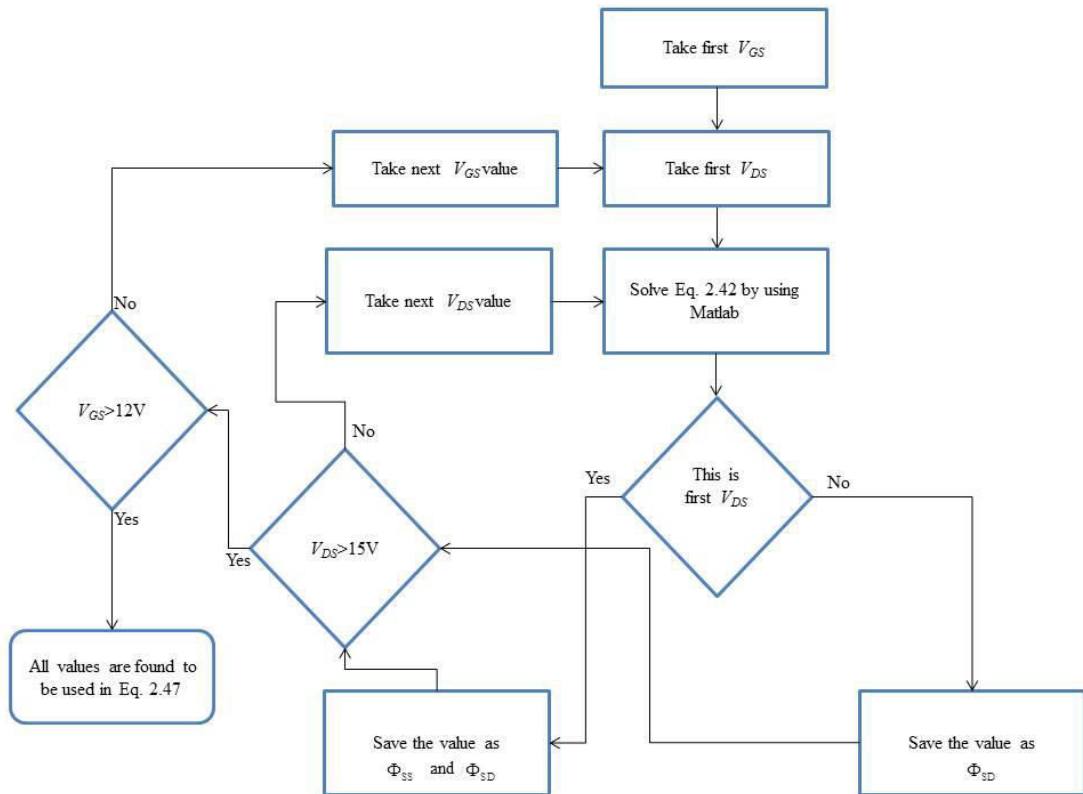


Figure 8 Φ_{SS} and Φ_{SD} calculation process

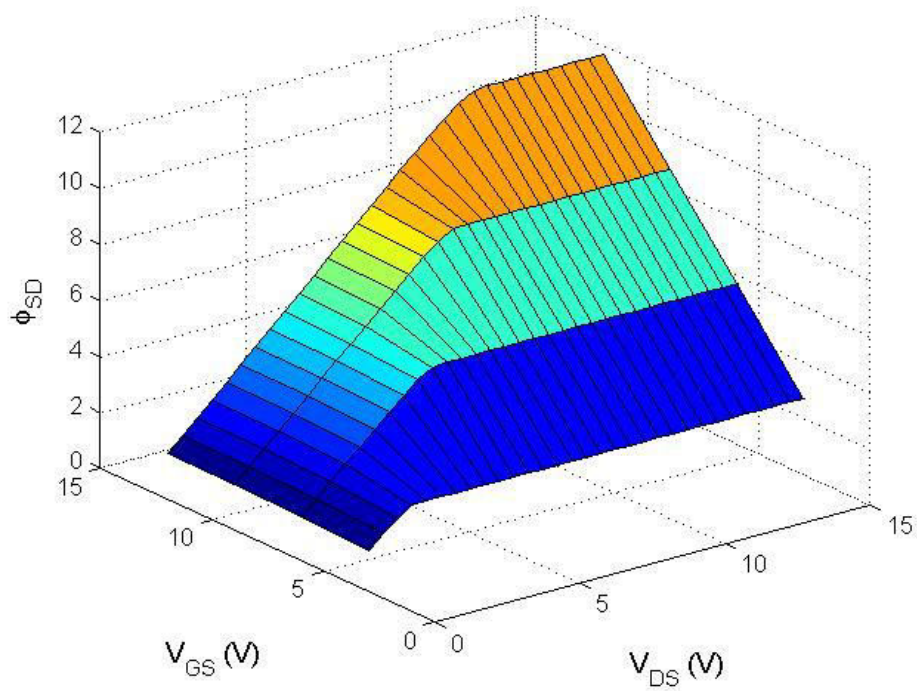


Figure 9 Φ_{SD} , V_{GS} and V_{DS} relation

The dependence of Φ_{SD} on V_{GS} and V_{DS} is shown in Fig. 9. As can be seen in the figure, V_{DS} is between from 0 and 15V . However, Φ_{SS} is obtained for $V_{DS} = 0$.

To verify if we derived everything correctly and properly we calculated the I_{DS} versus V_{DS} values with V_{GS} as parameters by using the values given in Table 2.1. and compared all these results with Minkyung Bae et al. [18]. The Output Characteristics that we obtain are shown in Fig. 10 to 12. As seen our values fit very well with their results. Therefore we confirm that all the derivations we have made are correct and also our flowchart for solving the static characteristics for the a-IGZO TFT is working.

As seen in Fig. 12 this model [18] works better than the gradual channel approximation because in his model one equation simulates the behavior of the transistor in all the regions (sub-threshold, and above threshold regions (linear and saturation regions)). However, in this model, solving Φ_S in terms of V_{GS} and V_{DS} in the nonlinear equation of 2-42, needs a numerical root-finding technique. In that sense this model of [18] can be more precisely a semi-analytic model.

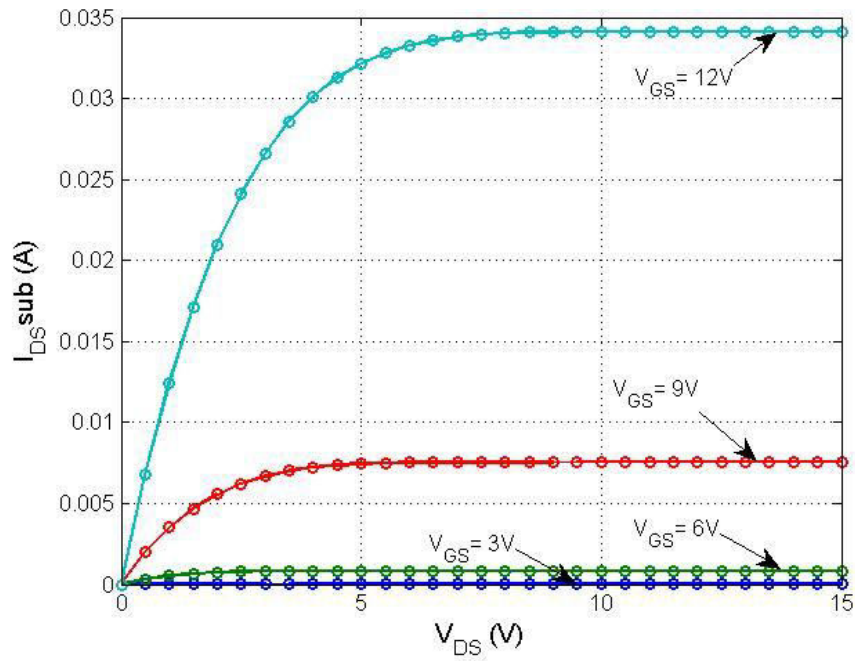


Figure 10 Drain to source current curves in sub-threshold region for the TFT having the parameters listed in Table 2.1 (lines are used for guiding eyes only)

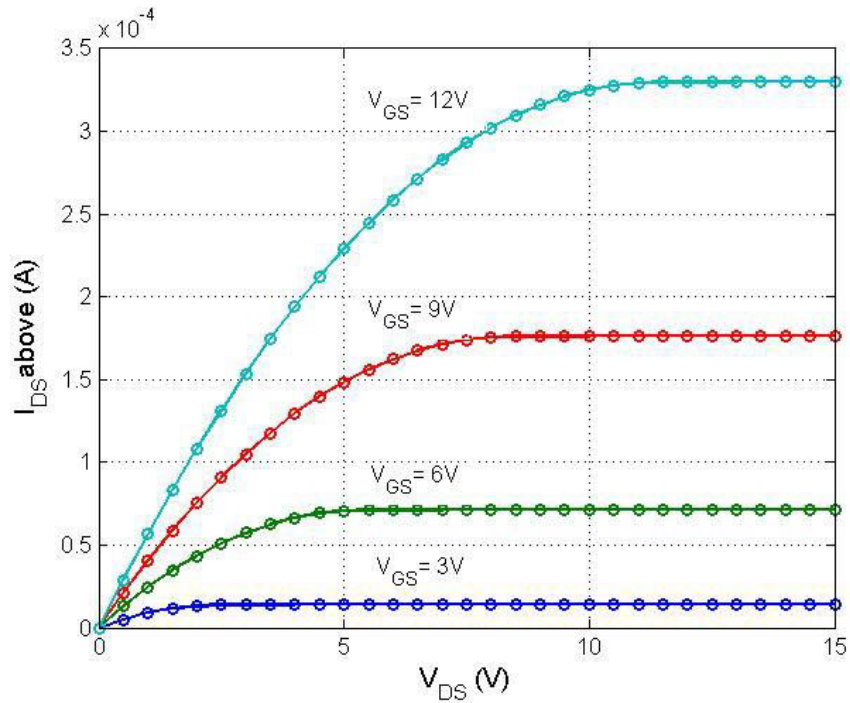


Figure 11 Drain to source current curves in above-threshold region for the TFT having the parameters listed in Table 2.1 (lines are used for guiding eyes only)

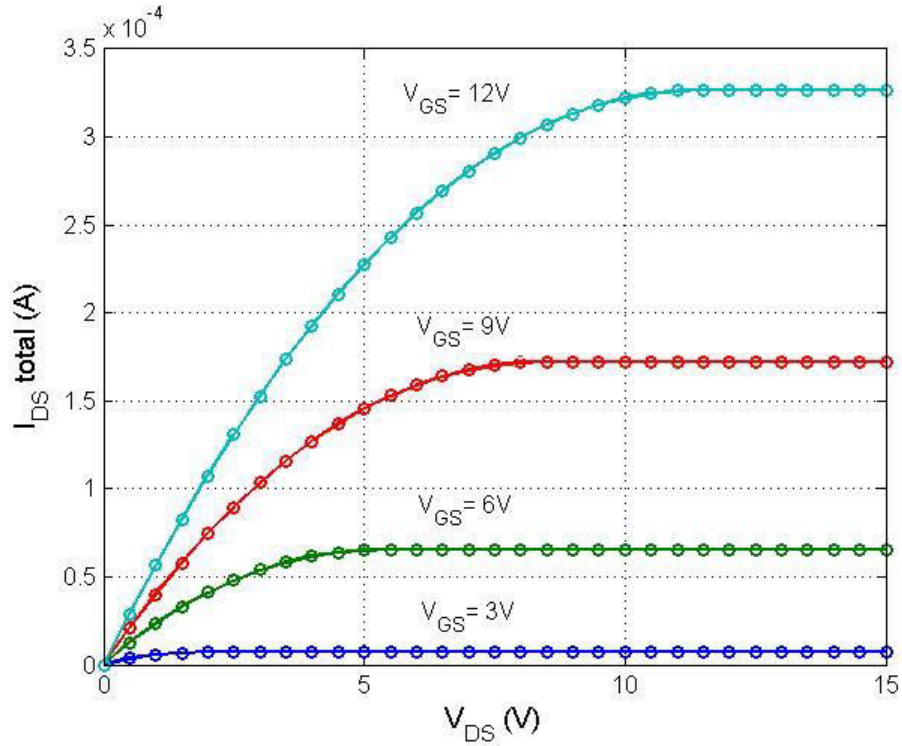


Figure 12 Total drain to source current curves (both sub and above threshold regions) for the TFT having the parameters listed in Table 2.1 (lines are used for guiding eyes only)

Fig. 12 is the same with the graphics that is given in [18]. We have produced these graphs by applying the flow chart above. If noticed, Fig. 11 and Fig. 12 look very similar. Since the current values that are found in the sub-threshold region for the same V_{GS} and V_{DS} values are higher than those obtained in the above-threshold region, considering Eq. 2.48, smaller I_{DS} 's are dominant in determining the overall I_{DS} 's.

When we verified that our equations, flowchart and the method of calculation are correct and accurate in calculating the static characteristic curves of the a-IGZO TFT we decided to check the effects of some parameters in Table 2.1 on the calculated

values. Since the values like N_{EFF1} , kT_{EFF1} , N_{EFF2} , kT_{EFF2} are estimated and used in the model as inputs we decided to analyze the sensitivity of the model on these parameters. We changed their values only 5% and generated the same curves as Fig. 12 for these values. When we changed N_{EFF1} and kT_{EFF1} , the density of the tail states and the activation energy of these states, respectively, 5% from their values in Table 2.1 the output characteristics did not change at all. However, a 5% change in N_{EFF2} and kT_{EFF2} , the density of deep states and the activation energy of these states, respectively, from their values given in Table 2.1 the output characteristics change considerably. Fig. 13 and 14 display the changes in the characteristics for a 5% change in N_{EFF2} and 5% change in kT_{EFF2} . From the figures one can easily see that the drain current values increase nearly 20% for a 5% decrease in N_{EFF2} (when we take $N_{EFF2} = 4.89 \times 10^{18} \text{ cm}^{-3}$ instead of $5.15 \times 10^{18} \text{ cm}^{-3}$); whereas, the drain current values decrease nearly 1100% for a 5% decrease in kT_{EFF2} (when we take $kT_{EFF2} = 0.0250 \text{ eV}$ instead of 0.0263 eV). Therefore, we believe that such level of error in estimating these values could be made very easily, and the sensitivity of the model to small changes in these values is the weakness of the model.

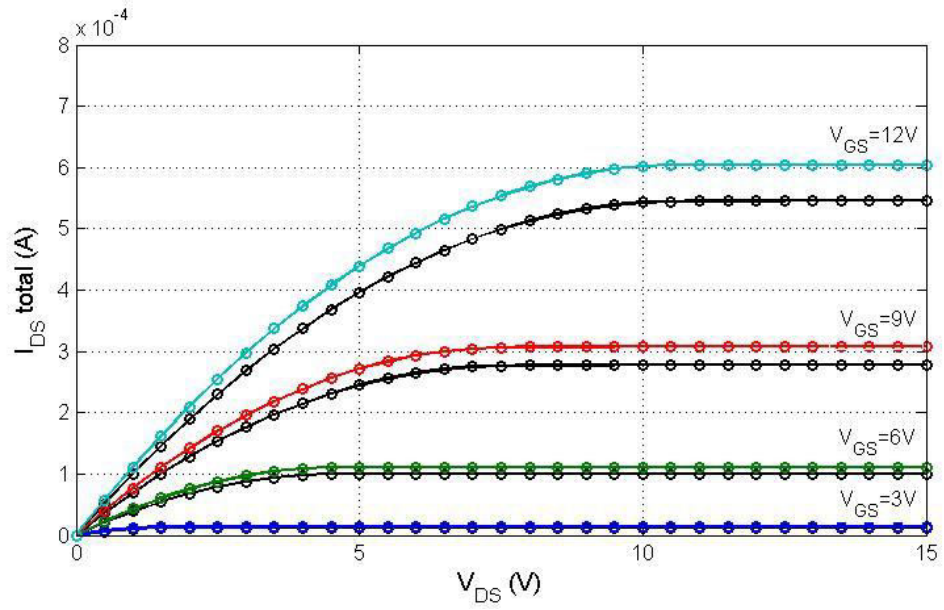


Figure 13 Changes in the characteristics for a 5% change in N_{EFF2} (curves in black color are the original curves, and the other curves for various colors are for decreased N_{EFF2} value)

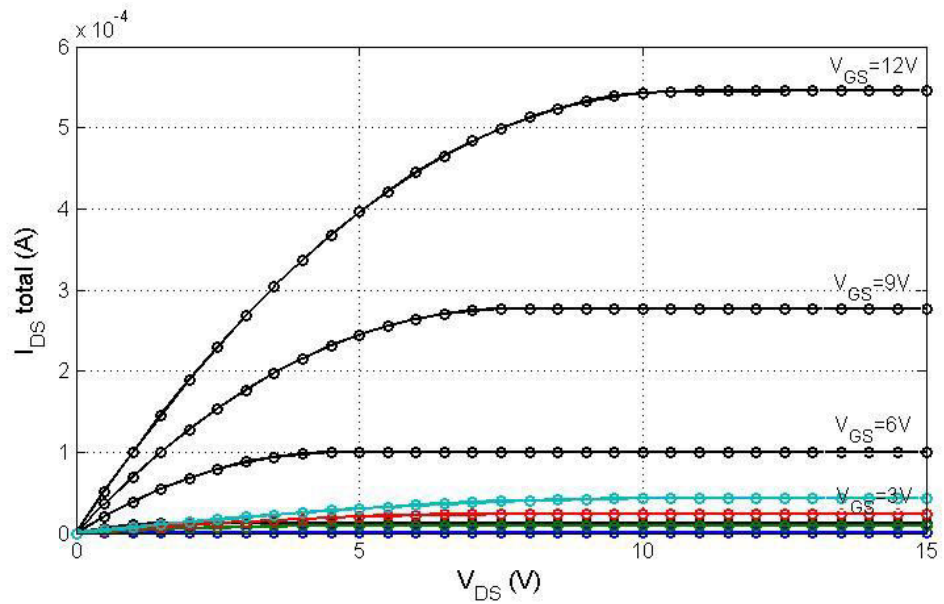


Figure 14 Changes in the characteristics for a 5% change in kT_{EFF2} (curves in black color are the original curves, and the other curves for various colors are for decreased kT_{EFF2} value)

CHAPTER 3

3. NEW SURFACE POTENTIAL-BASED ANALYTIC IGZO TFT MODEL

The Gradual Channel Approximation that we reviewed in Chapter 2 in modeling the FET, assuming constant channel mobility, is very practical because it is very simple, analytical, and quite successfully fits the empirical FET I-V behavior. However, it has different expressions for the different regions of the FET operation (one formula for the linear region, and another formula for the saturation region). On the other hand, it does not include any expression for the sub-threshold region at all. The same model has been used for a-Si:H TFTs by many authors. However, one analytical model to estimate all regions of the FET operation has always been needed.

Actually, the first analytical model for an a-Si:H TFT was introduced by Hack and Shur [41]. They obtained the channel conductance by a Taylor Series expansion, where they again developed different formulas for different operating regions of the transistor. They did not have one formula valid for all the regions of the TFT.

A unique formulation for the sub-threshold, above-threshold (linear and saturation) regions of an TFT, which accounts for a realistic distribution of tail and deep density of states (DOS) in the energy gap was developed by Colalongo [42]. This model is based on the charge-sheet analytical model of Brews for a crystalline metal-oxide-

semiconductor FET [43]. Colalongo adapted and generalized this model for a-Si:H TFTs to include the effect of trap states, namely tail and deep states, within the bandgap of hydrogenated amorphous silicon material. His model includes the relationship between the surface and the quasi-Fermi potential. One of the advantages of the model is that explicit definitions of the threshold and saturation voltages as input parameters, which cannot be accurately defined for these devices, are not required. In his model, he used constant channel mobility in calculating the drain current. However, in fitting his equations with the experimental data he took a mobility value of $10 \text{ cm}^2 / \text{Vs}$ which is very high and seems not attainable for an a-Si:H TFT [42]. If one considers that a-Si:H mobilities are less than $1 \text{ cm}^2 / \text{Vs}$, that is an order less than what he used, one concludes that his model underestimates the drain current values.

At this point we believe that we should first talk about the mobility of the charge carriers in the FET's channel. Mobility is the ease with which the charge carriers in the material move under the effect of a force. In the FETs we have two kinds of mobility: the field effect mobility and the band mobility. The field effect mobility (μ_{EFF}) in the induced channel, sometimes called as the channel mobility (μ_{CH}), of an FET of a crystalline semiconductor is equal to the conduction band mobility (μ_{BAND}), which is generally constant, because in a crystalline semiconductor the charge carriers are the free carriers in the conduction band (n_{FREE}). These carriers are induced in the channel with the applied gate to source voltage (V_{GS}). However, in the TFTs the channel materials are generally non-crystalline. These non-crystalline materials are either amorphous semiconductors (a-Si:H) or polycrystalline

semiconductor (poly-Si), or metal oxides (ZnO , $CdSe$ or a-IGZO), which are amorphous too. In non-crystalline semiconductors the charge carriers, for example electrons, are not only those from the conduction band (n_{FREE}), but those from the localized states within the bandgap (n_{LOC}) as well. The field effect mobility in non-crystalline semiconductors is, thus, generally a function of the channel potential $V_{CH}(y)$, and given in one approach [19,44,45,46] as we used in Chapter 2 in deriving their formulation in detail:

$$\mu_{EFF} = \mu_{BAND} \frac{Q_{FREE}(x, V_{CH}(y))}{Q_{FREE}(x, V_{CH}(y)) + Q_{LOC}(x, V_{CH}(y))} \quad (2.31)$$

where Q_{FREE} is the total free charge density, and Q_{LOC} is the total localized charge density in the channel, x being the transverse distance from the gate oxide surface, $V_{CH}(y)$ is the channel potential at y , y being the distance from source to drain. $V_{CH}(y)$ is determined by V_{GS} and V_{DS} . In a-Si:H material since $Q_{LOC} \gg Q_{FREE}$ the field effect mobility is much less than the band mobility, and therefore the mobility in a-Si:H TFTs channel, μ_{EFF} , is nearly constant or a weak function of $V_{CH}(y)$ [44]. However, in poly-Si or in a-IGZO the total charge of free carriers are comparable with the total charge of the localized carriers or even larger, and the field effect mobility can get a values that are somewhat closer to the band mobility. Moreover, in these TFTs the field effect mobility is a strong function of $V_{CH}(y)$.

Eq. 2.31 is an empirical approximation introduced to explain the difference of the field effect mobility from the band mobility in a TFT. This formula has been used by

some [18, 19] in their model for the a-IGZO TFTs for a quite wide range of I-V characteristics. Actually, in the model we analyzed in detail in Chapter 2, Minkyung Bae et al. [18] used the same approach to incorporate the tail and deep states in the band gap with Colalongo [42] in deriving the drain current for sub-threshold and above-threshold regions; however, since a-IGZO has free carriers contributing to the channel conductivity considerably, they used n_{FREE} as well in addition to the localized states and also they, like Colalongo, introduced a channel potential dependence on the channel mobility.

In some other works, the mobility's dependence on channel potential $V_{CH}(y)$ is modeled by another formula [45,47-50]

$$\mu_{EFF} = \mu_{BAND} \left(\frac{V_{GS} - V_T}{V_{AA}} \right)^\gamma \quad (3.1)$$

where V_T is the threshold voltage, V_{AA} is a fitting voltage and γ is another fitting parameter. It was used with a success to some extent for a-Si:H TFTs, since their mobilities are weakly dependent on $V_{CH}(y)$. This formula was not preferred for the a-IGZO TFTs because in those TFTs mobilities are somewhat stronger function of $V_{CH}(y)$.

In his work for TFTs Tze-Ching Fung [21] used the gradual channel approximation but with a gate-to-source voltage dependent mobility to model the a-IGZO TFT. He introduced the channel mobility as

$$\mu_{EFF}(V_{GS}) = \mu_0 \left[\frac{V_{GS} - V_T}{V_C} \right]^\alpha \quad (3.2)$$

where μ_0 is the intrinsic band mobility, V_C is the material-dependent critical voltage, and α is a coefficient which describes the dependence of mobility μ_{EFF} on $(V_{GS} - V_T)$. Then, in the simplified form he expressed the mobility as

$$\mu_{EFF}(V_{GS}) = K (V_{GS} - V_T)^{\gamma-1} \quad (3.3)$$

where K is a material dependent parameter as $K = \mu_0 (1/V_C)^\alpha$, and $\gamma = \alpha + 1$.

The drain current in the Gradual Channel Approximation, using a voltage-dependent mobility in the linear region can be expressed as

$$I_D = K Cox(W/L) (V_{GS} - V_T)^\gamma V_{DS} \quad (3.4)$$

He also defined the incremental mobility

$$\mu_{inc} = \left(\frac{\delta I_D}{\delta V_{GS}} \right) \left[\frac{L}{WCoxV_{DS}} \right] \quad (3.5)$$

where L is the channel length and W is the channel width of the TFT. And, from Eq. 3.4 and Eq. 3.5 he obtained the incremental mobility as

$$\mu_{inc} = K \gamma (V_{GS} - V_T)^{\gamma-1} \quad (3.6)$$

Fig. 15 shows the incremental mobility dependence on the gate-to-source voltage extracted from the measured I_D versus V_{GS} curve from an a-IGZO TFT [21].

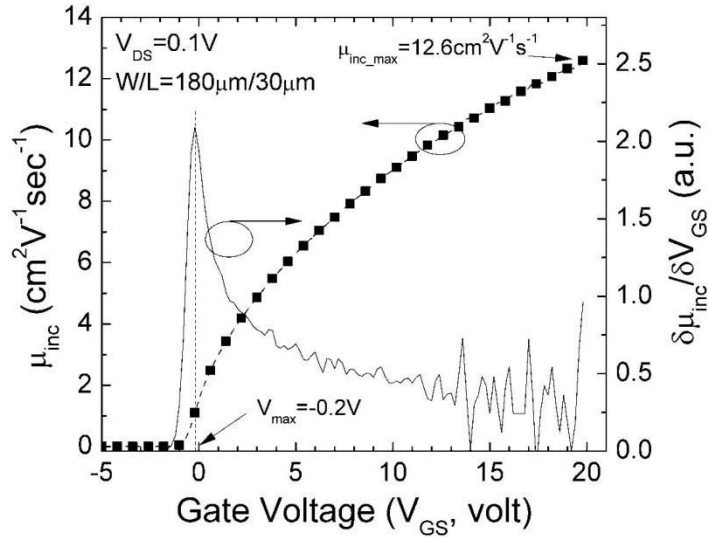


Figure 15 Incremental field effect mobility (μ_{inc}) of an a-IGZO TFT [21]

The extracted μ_{inc} is a strong function of V_{GS} and reaches a maximum value of $12.6 \text{ cm}^2 / Vs$, and μ_{inc} does not saturate. Such behavior was also observed in other oxide semiconductors [51,52]. The γ value here extracted, by linear fitting, from the experimental curves is equal to 1.52.

As we redeveloped all the equations for the model in [18] in Chapter 2 again and obtained the values of I_{DS} versus V_{GS} and V_{DS} by using their parameters given in their manuscript, we showed that the model using Eq. 2.31 is very sensitive to parameters N_{EFF2} 's and kT_{EFF2} , that are either extracted from the experimental characteristics or estimated. We noticed that even very small change on these parameters cause very big changes in the I-V curves. For example a change in N_{EFF2} from 5.15×10^{18} to 4.89×10^{18} , causes a 20% increase in I_{DS} , whereas, I_{DS} values

decrease nearly 1100% for a 5% decrease in kT_{EFF2} (when we take kT_{EFF2} 0.0250 eV instead of 0.0263 eV). Since it is nearly impossible to experimentally determine or estimate these parameters about this level of accuracy, and the model's success is solely dependent on selecting these parameters that accurate in the beginning, we thought that we could introduce another model for mobility. By considering the results and findings of [21] about the dependence of the mobility on the V_{GS} , and by considering Eq. 2.31 for the mobility dependence on the channel voltage $V_{CH}(y)$ in their model [18], and by comparing their results with the measured values given, we think that a new formula for the mobility dependence on the channel voltage, and an average of all the carriers contributing to the conduction process in the channel (carriers from free and localized states) would produce a better model for an a-IGZO TFT.

Towards this goal, we first checked the empirical formula Eq. 3.1 to estimate the I-V characteristics for an a-IGZO TFT. We tried a range of constant values for either V_{AA} and for γ and saw that they were not effective to fit the experimental I-V values of the TFT. Therefore, we introduced a new formula inspired from this equation as:

$$\mu_{EFF} = \mu_{BAND} \left[\frac{(V_{GS} - V_T)}{V_{AA}} \right]^{\gamma(V_{GS}, V_{DS})} \quad (3.7)$$

Here γ is not constant as in Eq. 3.3 but a function of V_{GS} and V_{DS} , and V_{AA} is a fix voltage to provide unit consistency. We used the same approach as given in [5,18,42] developing our model to estimate the I-V characteristics of an a-IGZO TFT, not by using Eq. 2.31 as they did in [18] but by using our formula Eq. 3.7 for the effective

mobility. This γ , to be determined in mobility equation, Eq. 3.7, is not a constant as in Eq. 3.1 but a function of both V_{GS} and V_{DS} , that is $V_{CH}(y)$.

Jun Hyung Park et al. introduced another model [17], where they also used Eq. 2.31 for mobility but instead of differentiating tail states and deep states for the localized states and used N_{EFF} 's (N_{EFF1}, N_{EFF2}) and characteristic slopes (activation energies) for each of them (kT_{EFF1}, kT_{EFF2}) as Minkyung Bae et al., they took only one localized carriers of N_{EFF} and one characteristic slope kT_{EFF} . They even went one step further and represented all carriers in the channel with effective carriers (n_{EFF}), which is the sum of the free carriers (n_{FREE}) from the conduction band and localized carriers (n_{LOC}) from the states in the bandgap. Although we did not use their approach for mobility, we used the same approach of representing all the carriers contributing conduction in the channel as effective carriers (n_{EFF}).

Since the potential in the TFT's channel is not only determined by V_{GS} but V_{DS} as well, the mobility should also dependent on V_{GS} and V_{DS} . We believe that our formula, Eq. 3.7, for mobility in this sense is more realistic in representing the channel mobility than the other models cited above.

3.1. Developing Our Model for an a-IGZO TFT

As we stated above we start with a new formula for the channel mobility to derive our model

$$\mu_{CH} = \mu_{BAND} \left(\frac{V_{GS} - V_T}{V_{AA}} \right)^\gamma \quad (3.8)$$

We assume that there is no dependence of μ_{CH} on geometry. In other words, if there is a specific difference of TFT in geometrical features, this will be reflected into given parameters.

Eq. 2.34 gives the relation between effective channel mobility and I_{DS} . So, we combine Eq. 2.34 and Eq. 3.8

$$I_{DS} = W \frac{dV_{CH}}{dy} \int_{\Phi(x=T_{IGZO})}^{\Phi(x=0)} q \mu_{BAND} \left(\frac{V_{GS} - V_T}{V_{AA}} \right)^\gamma \frac{n_{FREE}(\Phi(x))}{E_{IGZO}(\Phi(x))} d\Phi(x) \quad (3.9)$$

By using the information given in Eq. 2.19, we can derive

$$E_{IGZO}(\Phi(x)) = \sqrt{\frac{2N_{EFF}kT_{EFF}}{\epsilon_{IGZO}}} \exp \left[\frac{q(\Phi(x) - \Phi_{FO} - \Phi_{CH})}{2kT_{EFF}} \right]. \quad (3.10)$$

Eq. 2.21 provides information about $n_{FREE}(\Phi(x))$. Using eq.2.21, and Eq.3.10 in Eq.3.9 we can obtain

$$I_{DS} = W q \mu_{BAND} \left(\frac{V_{GS} - V_T}{V_{AA}} \right)^\gamma \frac{dV_{CH}}{dy} \times \int_{\Phi(x=T_{IGZO})}^{\Phi(x=0)} \frac{N_c \exp \left[\frac{q(\Phi(x) - \Phi_{FO} - V_{CH}(y))}{kT} \right]}{\sqrt{\frac{2N_{EFF}kT_{EFF}}{\epsilon_{IGZO}}} \exp \left[\frac{q(\Phi(x) - \Phi_{FO} - \Phi_{CH})}{2kT_{EFF}} \right]} d\Phi(x) \quad (3.11)$$

While we are recombining Eq. 3.5 to make it easier to take an integral, we will use Eq. 2.27 to simplify the equation. When we make these changes

$$I_{DS} = \frac{Wq\mu_{BAND}N_c}{\sqrt{\frac{2N_{EFF}kT_{EFF}}{\epsilon_{IGZO}}}} \left(\frac{V_{GS} - V_T}{V_{AA}} \right)^\gamma \frac{dV_{CH}}{dy} \times \int_{\Phi(x=T_{IGZO})}^{\Phi(x=0)} \exp[qB^*(\Phi(x) - \Phi_{FO} - V_{CH}(y))] d\Phi(x) \quad , \quad (3.12)$$

$$\text{where } B^* = \left(\frac{1}{kT} - \frac{1}{2kT_{EFF}} \right).$$

The surface potential $\Phi(x=0) = \Phi_s$. In addition to this, we use the relation given in Eq. 2.44 to convert the integral dependence from Φ_s to y .

$$I_{DS} = \frac{Wq\mu_{BAND}N_c}{B^* \sqrt{\frac{2N_{EFF}kT_{EFF}}{\epsilon_{IGZO}}}} \left(\frac{V_{GS} - V_T}{V_{AA}} \right)^\gamma \left[1 + \frac{2kT_{EFF}}{q(V_{GS} - V_{FB} - \Phi_s)} \right] \times \exp[qB^*(\Phi_s - \Phi_{FO} - V_{CH}(y))] \frac{d\Phi_s(y)}{dy} \quad (3.13)$$

By using Eq. 2.42, we can convert I_{DS} equation into Eq. 3.14.

$$I_{DS} = \frac{Wq\mu_{BAND}N_c}{B^* \sqrt{\frac{2N_{EFF}kT_{EFF}}{\epsilon_{IGZO}}}} \left(\frac{V_{GS} - V_T}{V_{AA}} \right)^\gamma \left[1 + \frac{2kT_{EFF}}{q(V_{GS} - V_{FB} - \Phi_s)} \right] \times \exp \left\{ B^* 2kT_{EFF} \ln \left[\frac{C_{OX}(V_{GS} - V_{FB} - \Phi_s)}{\sqrt{2\epsilon_{IGZO}N_{EFF}kT_{EFF}}} \right] \right\} \frac{d\Phi_s(y)}{dy} \quad (3.14)$$

We got rid of $V_{CH}(y)$ by this way. After making some simplifications in Eq. 3.14., we obtain

$$I_{DS} = \frac{Wq\mu_{BAND}N_c}{B^* \sqrt{\frac{2N_{EFF}kT_{EFF}}{\epsilon_{IGZO}}}} \left(\frac{V_{GS} - V_T}{V_{AA}} \right)^\gamma \left[1 + \frac{2kT_{EFF}}{q(V_{GS} - V_{FB} - \Phi_S)} \right] \times \left[\frac{C_{OX}(V_{GS} - V_{FB} - \Phi_S)}{\sqrt{2\epsilon_{IGZO}N_{EFF}kT_{EFF}}} \right]^{\left(\frac{2kT_{EFF}}{kT} - 1\right)} \frac{d\Phi_S(y)}{dy} \quad . (3.15)$$

If we take the integral along the channel (from $y = 0$ to $y = L$)

$$I_{DS} \int_0^L dy = \frac{Wq\mu_{BAND}N_c}{B^* \sqrt{\frac{2N_{EFF}kT_{EFF}}{\epsilon_{IGZO}}}} \left(\frac{V_{GS} - V_T}{V_{AA}} \right)^\gamma \times \left\{ \int_{\Phi_S(y=0)}^{\Phi_S(y=L)} \left[\frac{C_{OX}(V_{GS} - V_{FB} - \Phi_S)}{\sqrt{2\epsilon_{IGZO}N_{EFF}kT_{EFF}}} \right]^{\left(\frac{2kT_{EFF}}{kT} - 1\right)} d\Phi_S(y) + \int_{\Phi_S(y=0)}^{\Phi_S(y=L)} \left[\frac{2kT_{eff}}{q(V_{GS} - V_{FB} - \Phi_S)} \right] \left[\frac{C_{OX}(V_{GS} - V_{FB} - \Phi_S)}{\sqrt{2\epsilon_{IGZO}N_{EFF}kT_{EFF}}} \right]^{\left(\frac{2kT_{EFF}}{kT} - 1\right)} d\Phi_S(y) \right\} \quad . (3.16)$$

Here we have a sum of two integrals, which can be called as I_1 and I_2 .

$$I_{DS} \int_0^L dy = \frac{Wq\mu_{BAND}N_c}{B^* \sqrt{\frac{2N_{EFF}kT_{EFF}}{\epsilon_{IGZO}}}} \left(\frac{V_{GS} - V_T}{V_{AA}} \right)^\gamma \times (I_1 + I_2) \quad (3.17)$$

When we take the first integral in Eq. 3.16, the result is

$$I_1 = \left(\frac{C_{OX}}{\sqrt{2\varepsilon_{IGZO} N_{EFF} kT_{EFF}}} \right)^{\left(\frac{2kT_{EFF}-1}{kT} \right)} \left(\frac{kT}{2kT_{EFF}} \right) \times \left[(V_{GS} - V_{FB} - \Phi_{SS})^{\left(\frac{2kT_{EFF}}{kT} \right)} - (V_{GS} - V_{FB} - \Phi_{SD})^{\left(\frac{2kT_{EFF}}{kT} \right)} \right]. \quad (3.18)$$

When we calculate the second integral, the result is

$$I_2 = \left(\frac{2kT_{EFF}}{q} \right) \left(\frac{C_{OX}}{\sqrt{2\varepsilon_{IGZO} N_{EFF} kT_{EFF}}} \right)^{\left(\frac{2kT_{EFF}-1}{kT} \right)} \frac{1}{\left(\frac{2kT_{EFF}}{kT} - 1 \right)} \times \left[(V_{GS} - V_{FB} - \Phi_{SS})^{\left(\frac{2kT_{EFF}-1}{kT} \right)} - (V_{GS} - V_{FB} - \Phi_{SD})^{\left(\frac{2kT_{EFF}-1}{kT} \right)} \right]. \quad (3.19)$$

If we insert I_1 and I_2 into (3.16), the final expression is obtained as

$$I_{DS} = \frac{W}{L} \frac{q\mu_{BAND} N_c}{B^* \sqrt{2\varepsilon_{IGZO} N_{EFF} kT_{EFF}}} \left(\frac{V_{GS} - V_T}{V_{AA}} \right)^\gamma \left(\frac{C_{OX}}{\sqrt{2\varepsilon_{IGZO} N_{EFF} kT_{EFF}}} \right)^{\left(\frac{2kT_{EFF}-1}{kT} \right)} \times \left\{ \left(\frac{kT}{2kT_{EFF}} \right) \left[(V_{GS} - V_{FB} - \Phi_{SS})^{\left(\frac{2kT_{EFF}}{kT} \right)} - (V_{GS} - V_{FB} - \Phi_{SD})^{\left(\frac{2kT_{EFF}}{kT} \right)} \right] + \left(\frac{2kT_{EFF}}{q} \right) \frac{1}{\left(\frac{2kT_{EFF}}{kT} - 1 \right)} \times \left[(V_{GS} - V_{FB} - \Phi_{SS})^{\left(\frac{2kT_{EFF}-1}{kT} \right)} - (V_{GS} - V_{FB} - \Phi_{SD})^{\left(\frac{2kT_{EFF}-1}{kT} \right)} \right] \right\} \quad (3.20)$$

This equation is the main equation of our model that gives the relation between I_{DS} , V_{GS} and V_{DS} . We compared the calculations from this equation firstly with the model that is more similar to our model then the model in [18] in the sense that it also uses

the n_{EFF} for the number of carriers taking part in the channel conduction process for an a-IGZO TFT [17], however, differing from our model in modeling the mobility. In [17] Park et al. used exactly the same formulations as we analyzed in Chapter 2 in detail, however, they used only one N_{EFF} and kT_{EFF} for an effective carrier concentration n_{EFF} . Therefore, to make the comparison we took the same parameter values as used by Park et al. [17], shown in Table 3.1.

Parameter	Value	Parameter	Value
W / L [μm]	200/50	N_{EFF} [m^{-3}]	3.12×10^{18}
μ_{BAND} [$\text{cm}^2 / \text{V}\cdot\text{s}$]	17.4	kT_{EFF} [eV]	0.028
N_C [cm^{-3}]	3×10^{18}	C_{OX} [nF/cm^2]	42.37
V_{FB} [V]	0.2	ϕ_{F0} [V]	0.5
V_{AA} [V]	1	V_T [V]	0.6

Table 3 Geometrical and extracted model parameters [17]

Using these values, we calculated the output characteristics of the TFT and generated Fig. 16 with Eq. 3.20, by using $\gamma = 0.06$ as used by [19].

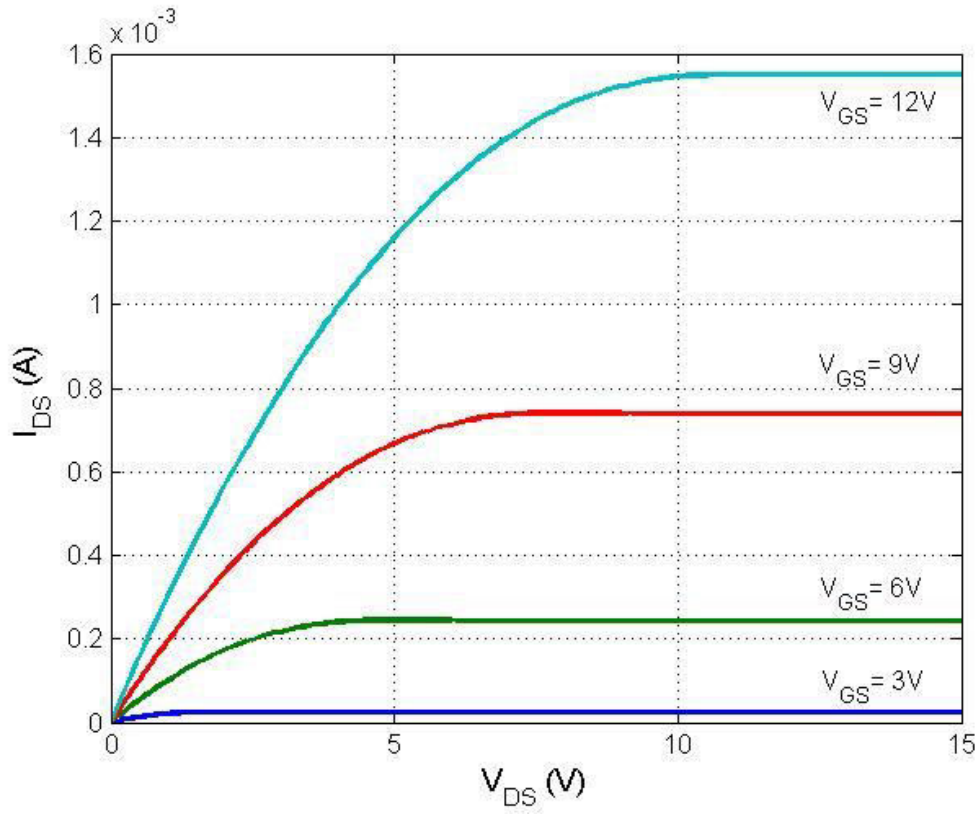


Figure 16 I_{DS} curves by using Eq. 2.47

To compare the results from our formula with the model by [17], we calculated the I_{DS} values, by changing V_{GS} and V_{DS} using Eq. 2.47 (Park et al.'s formulation) with the same parameter values given in Table 3.1. We obtained Fig. 17.

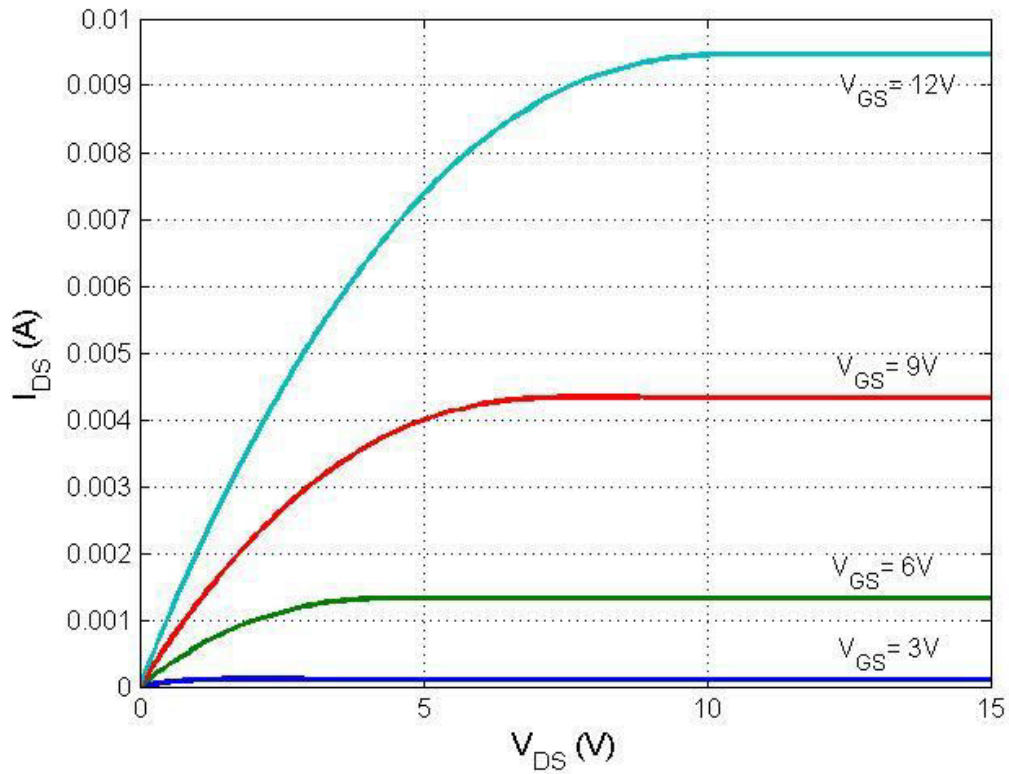


Figure 17 I_{DS} curves by using Eq. 3.20

When we compare Fig. 16 and Fig. 17, we can see that although the general behaviors of the curves are the same, the numerical values are at least an order of different. This is due to the reason that we took a constant γ value. However, as we explained above, our γ is a function of V_{GS} and V_{DS} . We need to determine the best function for γ to successfully fit the TFT characteristics.

3.2. Fitting Theoretical Parts with Experimental Values

In finding a proper function to represent γ , we used the measured data of the TFTs available in the literature. We found the measured data in the figures from the manuscripts in the literature but we needed to accurately transcribe the correct numerical values from the figures. We used some image processing to obtain the

numerical data values from the figures. Fig 3.4 shows the output characteristics of an a-IGZO TFT from measured data given by Minkyung Bae et al. [18]. We obtained the numerical values from Fig. 18 by applying the image processing methods to form our measured data set.

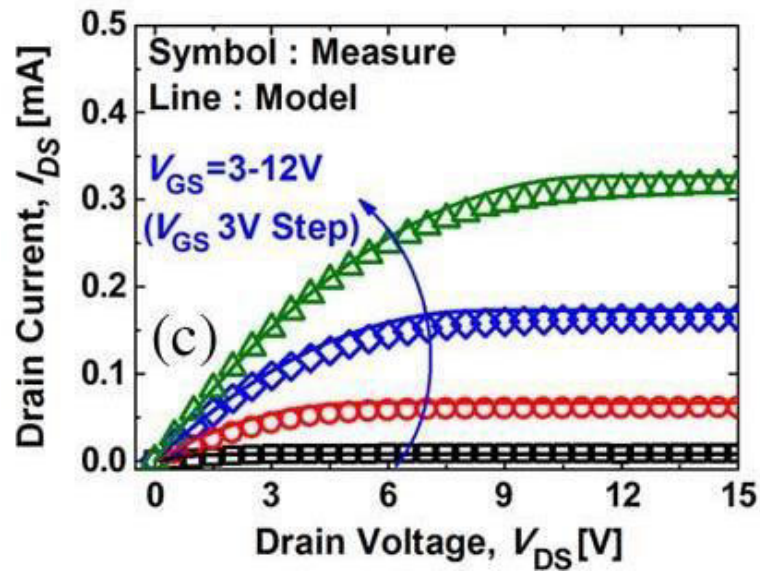


Figure 18 $I_{DS} - V_{DS}$ graphics (output characteristics) of an a-IGZO TFT from [18]

used to obtain the measured data values for our model verification

In the graphic given in Fig. 18, symbols show the measured data values. It is not easy to get numerical values by eye inspection, and moreover, we need to have accurate data values to be compared properly with our model values. So, we used image processing methods and got numerical values. The derived numerical values are given in Table 3.2.

$V_{GS}=12V$		$V_{GS}=9V$		$V_{GS}=6V$		$V_{GS}=3V$	
V_{DS} (v)	I_{DS} (mA)	V_{DS} (v)	I_{DS} (mA)	V_{DS} (v)	I_{DS} (mA)	V_{DS} (v)	I_{DS} (mA)
0,465	0,0103	0,468	0,00948	0,624	0,00558	0,938	0,00727
0,95	0,0382	0,796	0,0231	0,874	0,0123	1,38	0,0117
1,43	0,0658	1,08	0,0348	1,14	0,0205	1,91	0,015
1,91	0,093	1,45	0,0489	1,46	0,0279	2,39	0,0161
2,39	0,116	1,91	0,0644	1,9	0,0359	2,86	0,0171
2,89	0,14	2,42	0,0806	2,38	0,0424	3,36	0,0181
3,36	0,161	2,9	0,0943	2,87	0,0484	3,85	0,0182
3,85	0,18	3,39	0,106	3,36	0,0538	4,33	0,0182
4,34	0,199	3,86	0,117	3,85	0,058	4,82	0,0182
4,83	0,215	4,34	0,127	4,33	0,0618	5,3	0,0182
5,31	0,23	4,83	0,135	4,82	0,0638	5,76	0,0182
5,79	0,244	5,8	0,148	5,29	0,0662	6,26	0,0185
6,27	0,255	6,29	0,153	5,79	0,0673	6,76	0,0185
6,75	0,267	6,77	0,157	6,27	0,0686	7,25	0,0185
7,24	0,277	7,25	0,161	6,75	0,0688	7,71	0,0185
7,72	0,285	7,74	0,163	7,24	0,0688	8,19	0,0185
8,21	0,292	8,22	0,165	7,71	0,0692	8,67	0,0188
8,7	0,298	8,7	0,167	8,21	0,0694	9,16	0,0188
9,18	0,303	9,2	0,168	8,69	0,0696	9,65	0,0188
9,66	0,306	10,6	0,17	9,16	0,0701	10,1	0,0188
10,2	0,311	11,1	0,171	9,64	0,0701	10,6	0,0188
10,6	0,313	12,1	0,172	10,1	0,0701	11,1	0,0188
11,1	0,315	12,6	0,172	10,6	0,0701	11,6	0,0188
11,6	0,317	13,1	0,172	11,1	0,0703	12,1	0,0188
12,1	0,318	13,6	0,172	11,6	0,0703	12,6	0,0191
12,6	0,32	14	0,172	12,1	0,0703	13,1	0,0191
13,1	0,32	14,5	0,172	12,6	0,0703	13,5	0,0191
13,5	0,322	14,9	0,172	13,1	0,0705	14	0,0191
14	0,322			13,5	0,0705	14,5	0,0191
14,5	0,322			14	0,0705	14,9	0,0191
14,9	0,322			14,5	0,0705		
				14,9	0,0705		

Table 4 The measured data values obtained from Fig. 18 by an image processing method (all data values are for 4 significant digits)

We then tried to best fit our model calculations to the measured data by changing γ .

To do this, first we analyzed γ dependency of our model. In order to determine the γ dependency on V_{GS} and V_{DS} we decided to fit the calculated I_{DS} values to the

experimental values given in Fig. 18. In doing this, we firstly used the image processing method and formed a data table (Table 3.2) from measured I_{DS} values for the applied V_{DS} and V_{GS} values given in Fig. 18. Secondly, we calculated I_{DS} values by using Eq. 3.20. Then, we compared it with measured value for the same V_{GS} and V_{DS} . If it is different, we changed γ value. We calculated I_{DS} with new γ and compared it with measured data again. We repeated this process until we caught the measured value within a tolerance we decided. Thus, we fitted all the measured data points as given in Table 3.2 with the values obtained by using Eq. 3.20 as shown in Fig. 20, by calculating a γ value that provides the best fit for each data point.

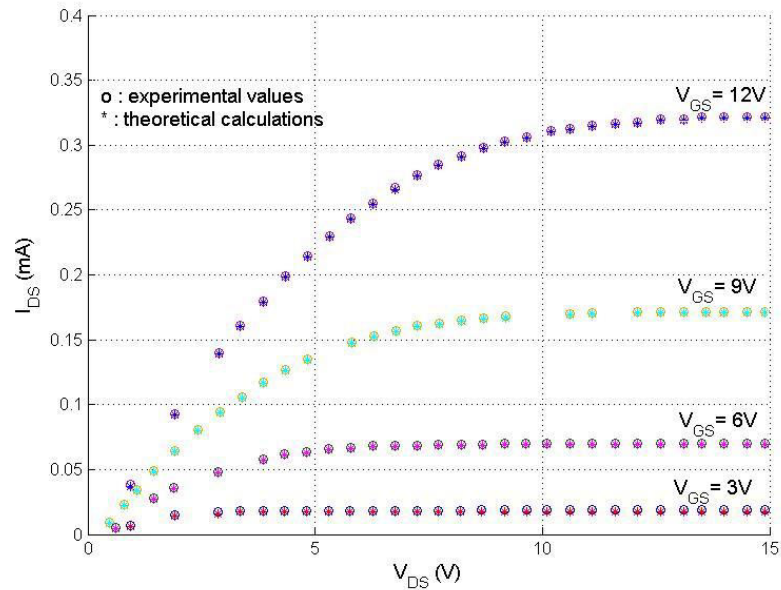


Figure 19 Experimental data and our model fitting by changing γ

In Fig 19, ‘o’ symbols show the measured data from Table 3.2. ‘*’ symbols denote the I_{DS} values that are calculated by best fitting I_{DS} values using Eq. 3.20 via changing γ . These γ values that make I_{DS} values best fit to the experimental data

are sketched in Fig. 20. We noticed from this figure that the biggest changes for γ occurred in the linear region of the I_{DS} versus V_{DS} curves in Fig. 18. For every measured data point in the linear region to fit, we needed a different γ value, as seen in Fig. 20.

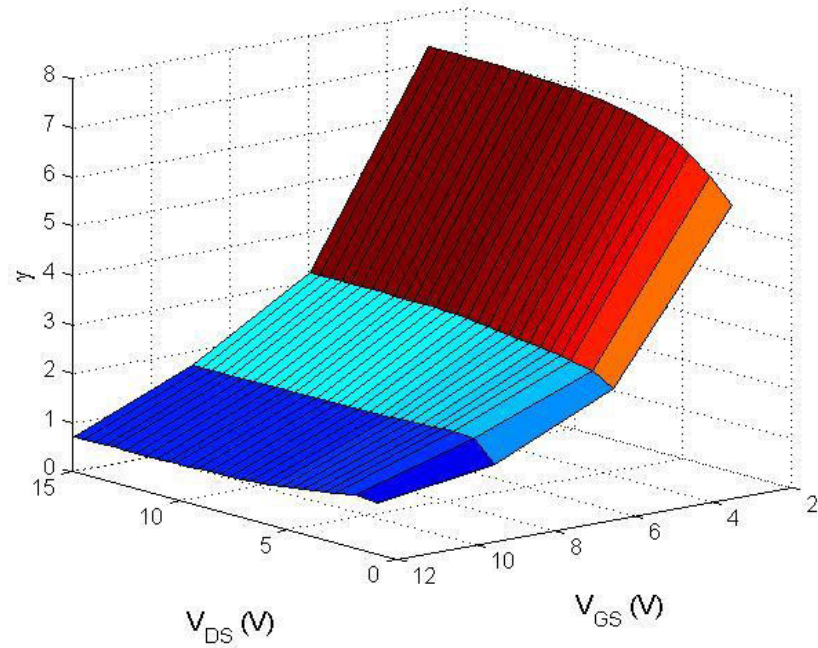


Figure 20 Drain and Gate voltage and best fitting γ relation

We developed a 2-D fitting equation for γ by using the Matlab's curve fitting tool for surfaces [53].

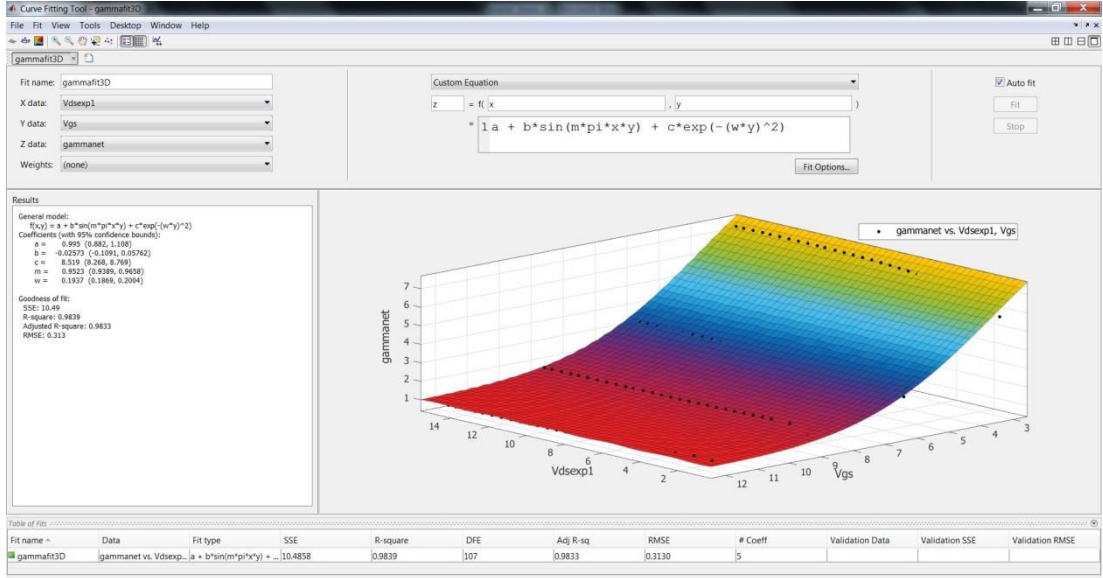


Figure 21 Snapshot of the custom equation surface fitting process screen

In fitting the 2-D equation to our 2-D surface in Fig. 20, we determined that a “custom equation” method in Matlab tools is the best way among others available. The fitted 2-D surface is given in Fig. 21. By using that method, we were able to find a function that expresses γ successfully as a function of V_{GS} and V_{DS} , given in the window of Fig. 21 as

$$\gamma = 1 - 0.025 \sin\left(\frac{\pi V_{GS} V_{DS}}{V_{AA}^2}\right) + 8.5e^{-\left(\frac{0.19V_{GS}}{V_{AA}}\right)^2} \quad (3.21)$$

When we combined Eq. 3.20 and Eq. 3.21, we found the final form of the I_{DS} equation of our model.

$$\begin{aligned}
I_{DS} = & \frac{W}{L} \frac{q\mu_{\text{BAND}} N_c}{B^* \sqrt{\frac{2N_{\text{EFF}}kT_{\text{EFF}}}{\epsilon_{\text{IGZO}}}}} (V_{\text{GS}} - V_{\text{T}})^{\left(1 - 0.025 \sin\left(\frac{\pi V_{\text{GS}} V_{\text{DS}}}{V_{\text{AA}}^2}\right) + 8.5 e^{-\left(\frac{0.19 V_{\text{GS}}}{V_{\text{AA}}}\right)^2}\right)} \\
& \times \left(\frac{C_{\text{OX}}}{\sqrt{2\epsilon_{\text{IGZO}} N_{\text{EFF}} kT_{\text{EFF}}}} \right)^{\left(\frac{2kT_{\text{EFF}} - 1}{kT}\right)} \\
& \times \left\{ \left(\frac{kT}{2kT_{\text{EFF}}} \right) \left[(V_{\text{GS}} - V_{\text{FB}} - \Phi_{\text{SS}})^{\left(\frac{2kT_{\text{EFF}}}{kT}\right)} - (V_{\text{GS}} - V_{\text{FB}} - \Phi_{\text{SD}})^{\left(\frac{2kT_{\text{EFF}}}{kT}\right)} \right] \right. \\
& \quad \left. + \left(\frac{2kT_{\text{EFF}}}{q} \right) \frac{1}{\left(\frac{2kT_{\text{EFF}}}{kT} - 1\right)} \right. \\
& \quad \left. \times \left[(V_{\text{GS}} - V_{\text{FB}} - \Phi_{\text{SS}})^{\left(\frac{2kT_{\text{EFF}} - 1}{kT}\right)} - (V_{\text{GS}} - V_{\text{FB}} - \Phi_{\text{SD}})^{\left(\frac{2kT_{\text{EFF}} - 1}{kT}\right)} \right] \right\} \quad (3.22)
\end{aligned}$$

This equation best fits our experimental values as shown in Fig. 19. The Matlab code to derive these current values is given in Appendix. Hence we derived a new formula for an a-IGZO TFT to estimate its static electrical characteristics. Our formula comprises an empirical model for the channel mobility (μ_{CH}) and based on the channel carrier concentration (n_{EFF}) dependence on the electrostatic potential, which is a function of V_{GS} and V_{DS} voltages. We used the approach taken by L. Colalongo [42], M. Bae et al. [18] and J. H. Park et al. [17], to solve the nonlinear equation to determine the electrostatic potential in the channel as a function of applied voltages. This model calculates the I_{DS} versus V_{DS} characteristics with one semi-analytic formula and does not need a different formula for each region. Our model differs from L. Colalongo and M. Bae et al. models in determining the mobility and the n_{EFF} in the channel. In their calculations they took the band tail states and midgap states that contribute to the carrier concentration as localized carriers (n_{LOC}) together

with the free carriers (n_{FREE}) in the conduction band of a-IGZO channel. However, in our model, like J. H. Park et al., we used only one type of carriers (n_{EFF}) with one characteristic slope (kT_{EFF}) to express the effective carrier concentrations in the channel together with the free carriers in the conduction band.

M. Bae et al. and J. H. Park et al. introduced a mobility model that is dependent of the free and localized carriers, however in our model we introduced a different empirical model for the channel mobility to enable us to 100% fit the model calculations of I_{DS} as a function of V_{GS} and V_{DS} if we have the experimental values available.

Our model is very powerful and flexible in the sense that if we have the experimental values of the I_{DS} as a function of V_{GS} and V_{DS} we can adjust our mobility formula to fit the I_{DS} values completely at every point of characteristics to the experimental values. Therefore, once one has the experimental characteristics of an a-IGZO TFT, using those data points in the measured data set we can adjust the best fitting mobility formula in our model for the specific TFT that we can 100% fit (our error range is 0.1%) to the DC I_{DS} values as a function of V_{GS} and V_{DS} . By using this formula afterwards, one can determine the circuit characteristics that are configured using the same type of TFTs as required. Yong et al. [54] reported that their static current model for an a-IGZO TFT could fit the voltage transfer characteristics (VTC) of an IGZO inverter, where two a-IGZO TFTs are used, within error ratio of 6%. We expect that a lower ratio of error than theirs could most probably be obtained in such an application if our model were used in the simulation. However, it should be

reminded that our model does not yet include the effect of the back potential between the channel and the substrate, as their model does.

CHAPTER 4

4. CONCLUSION

4.1. Conclusion

In this thesis we first analyzed the thin film transistors (TFTs) that are generally used as switching elements on large panel displays to switch the pixels on Liquid Crystal Displays (LCDs), light emitting diode (LED) displays, flexible displays, and on electronic paper and so on. These transistors have mostly an amorphous material for the channel. Amorphous hydrogenated silicon (a-Si:H) TFT was the first extensively used switching device because a-Si:H material is easy to deposit on a glass substrate at relatively low temperatures by using low-cost vacuum deposition techniques. However, it was found that a-Si:H is absorbing visible light photons and loses its stability in time. Recently a new amorphous metal oxide material of indium gallium zinc oxide (a-IGZO) has replaced the a-Si:H as the channel material in the TFTs due to its higher channel mobility, and better optical and electrical reliability.

We analyzed the material properties of a-Si:H and a-IGZO materials and the properties of TFTs made by using them. We discussed the requirements for a good TFT to drive the pixels on a flat panel display of different technologies, and the

channel material properties that meet these requirements mostly. We found that a-IGZO is the best material available for the TFTs today.

We then discussed the analytic models to describe the static electric characteristics of a TFT, which is a very similar device to a metal-oxide-semiconductor field effect transistor (MOSFET). We analyzed first the gradual channel approximation analytic model for a TFT. We pointed out that this model requires different expressions for each region of the transistor in the output characteristics, namely the sub-threshold, above-threshold, and saturation regions.

Searching for a better analytic model for an a-IGZO TFT, we analyzed a semi-analytic model for the TFT that estimates its behavior mainly by expressing the channel conductance as a function of the surface electrostatic potential, which is in turn dependent on the gate to source and drain to source voltages, V_{GS} and V_{DS} . We then indicated the importance for expressing the mobility of the channel in this model by relating it to the localized and free carriers in the amorphous materials.

We first reviewed Colalongo's [42] approach to model an a-Si:H TFT, where he used the tail and the deep states within the band gap of the amorphous silicon material to calculate the drain current using the charge-sheet analytical model. He used a constant mobility in deriving the drain current. We observed that his model needs rather high value of channel mobility ($10\text{cm}^2/Vs$) than measured for a-Si:H to fit the drain current predictions to the experimental data.

We then investigated Tze-Ching Fung's model for an a-IGZO TFT [21]. Fung used the gradual channel approximation to calculate the drain current. He used a channel

potential dependent mobility formula in his model. In his model he used different formulas of drain current for different regions of the TFT like gradual channel approximation, however, he introduced an empirical mobility expression in addition to better fit the predictions of the model to the experimental data.

Another analytic model was introduced by Minkyung Bae et al. [18] to represent the a-IGZO TFT static electrical behavior with one formula being valid in all the regions of operation. They used Colalongo's model of the drain current dependency of the localized states (tail states, and deep states), but they also add free carriers in their model because unlike the case for a-Si:H, in an a-IGZO free carrier concentration is also important. In addition to this, like Colalongo they used a mobility expression which is dependent on the carrier concentrations, that is, the channel potential. Their model incorporated tail states and deep states to represent the behaviors in sub-threshold and above-threshold regions of the TFT. We analyzed this model by deriving all the equations in the model in detail and developed the Matlab codes to solve the nonlinear equation to calculate the surface potential for the applied voltages. We verified that with our flowchart and codes we obtained the same values of drain currents for the applied voltages with theirs. We showed that their model is good in predicting the a-IGZO TFT behavior provided that the density of states in deep states (N_{EFF2}) and the characteristic slope (kT_{EFF2}) of the tail states are estimated very accurately, which seems impossible.

Jun Hyun Park et al. [17] introduced a new model following Minkyung Bae et al.'s way of development. The only difference they have from [18] is that instead of using tail and deep states and their specific activation energies for representing the channel

conductivity, they introduced an effective carrier density (n_{EFF}) with one effective density of states (N_{EFF}) and one effective activation energy (kT_{EFF}). However, for mobility they did the same thing as [18] and used the formula, namely they took

$$\mu_{EFF} = \mu_{BAND} \left[\frac{n_{FREE}}{(n_{FREE} + n_{LOC})} \right] \quad (4.1)$$

Although this model resolves somewhat the sensitivity of estimating the certain parameters, it is yet not predicting the behavior of the a-IGZO TFT's as accurately as [18] in all the operating regions of the TFT.

Then we developed a new analytic model for an a-IGZO TFT using the same approach as Jun Hyun Park, by taking only one effective carrier density (n_{EFF}) with one effective density of states (N_{EFF}), and one activation energy (kT_{EFF}) to calculate the drain current of the a-IGZO TFTs. However, unlike associating the channel mobility with the free and localized carrier densities as Minkyung Bae et al. and Jun Hyun Park et al. did, and associating the channel mobility with channel potential indirectly, we used an empirical formula that associates channel mobility with the channel potential directly, and derived the formulation to express I_{DS} with V_{GS} and V_{DS} . In this formulation, we improved the mobility expression by fitting the model's predictions with the measured data in an a-IGZO TFT. We used the best fitting mobility formula in our last equation. Our model strength comes from the fact that it is capable of fitting the experimental data nearly 100% by arranging our mobility formula.

This strength of our model could be employed in the applications where the model that predicts the behavior of the TFT is used in developing new circuits involving the many TFTs of the same or similar physical and geometric properties and simulating the overall behavior of the circuit prior to manufacturing. In this direction, an example case that Yong et al. [54] reported that they developed a numerical model for the static electrical behavior for an a-IGZO TFT and they used their model to fit the voltage transfer characteristics (VTC) of an a-IGZO inverter, where two a-IGZO TFTs are used, within error ratio of 6%. We expect that a lower ratio of error than theirs could most probably be obtained in such an application if our model were used in the simulation. However, it should be reminded that our model does not yet include the effect of the back potential between the channel and the substrate, as their model does.

4.2. Future Work Plan

Our last equation could be improved to include the back potential to make it suitable to use in the circuit simulations.

Our model predictions should be tested on simulating the device behavior, such as an inverter for instance, and the results should be benchmarked with the literature.

In developing and testing to improve our model, main problem we had was to find enough sample size of measured data from the TFTs of known physical and geometric parameters. We are planning to manufacture some a-IGZO TFTs in cooperation with the research groups elsewhere and make the required measurements to generate the required data set to improve our analytical model further.

REFERENCES

1. **Kuo Y. (2013)**, “*Thin Film Transistor Technology – Past, Present and Future*”, the Electrochemical Society Interface, pp. 55-61.
2. **Le Comber P. G., Spear W. E., Ghaith, A. (1979)**, “*Amorphous Silicon Field-Effect Device and Possible Application*”, Electronic Letters, vol. 15, no 6, pp. 179-181.
3. **Kagan C. R., Andry P. (2003)**, “*Thin Film – Transistors*”, IBM T. J. Watson Research Center, Yorktown Heights, New York.
4. http://en.wikipedia.org/wiki/Thin-film_transistor (Data Download Date: 22.07.2014)
5. **Streetman B. G., Banerjee S. K. (2009)**, “*Solid State Electronic Devices*”, Phi Learning, New Delhi.
6. **Chaji G. R., et. al., (2007)**, “*Electrical Compensation of OLED Luminance Degradation*”, IEEE Electron Device Letters, vol. 28, no 12, pp. 1108–1110.
7. **Chen H. C., et. al., (2007)**, “*a-Si Robust Gate Driver of 7.0-in. WVGA LCD Panel*”, in Proceeding SID Digital Technology Papers, pp. 222–225.
8. **Moon S. H., Lee, et. al., (2007)**, “*Integrated a-Si:H TFT Gate Driver Circuits on Large Area TFT-LCDs*”, in Proceeding SID Digital Technology Papers, pp. 1478–1481.
9. **Wager J. F., (2003)**, “*Transparent Electronics*”, Science, vol. 300, no 5623, pp. 1245-1246.

10. **Lin Y., Gundlach D. J., Nelson S. F., Jackson T. N., (1997)**, “*Pentacene-Based Organic Thin-film Transistors*”, IEEE Transactions on Electron Devices, vol. 44, no 8, pp. 1325-1331.
11. **Masuda S., et. al., (2003)**, “*Transparent Thin Film Transistors Using ZnO as an Active Channel Layer and Their Electrical Properties*”, Journal of Applied Physics, vol. 93, no 3, pp. 1624–1630.
12. **Hoffman R. L., Norris B. J., Wager J. F., (2003)**, “*ZnO-Based Transparent Thin-Film Transistors*”, Applied Physics Letters, vol. 82, no 5, pp. 733–735.
13. **Ohta Y., et. al., (2009)**, “*Amorphous In–Ga–Zn–O TFT-LCDs with High Reliability*”, in Proceeding International Display Workshop, pp. 1685–1688.
14. **Kamiya T., Nomura, K., Hosono, H., (2010)**, “*Present Status of Amorphous In-Ga-Zn-O Thin Film Transistors*”, Science and Technology of Advanced Materials, no 11, pp. 044305-044328.
15. **Sakata J., et. al., (2009)**, “*Development of 4.0-in. AMOLED Display with Driver Circuit Using Amorphous In–Ga–Zn–Oxide TFTs*”, in Proceeding International Display Workshop, pp. 689–692.
16. **Lee J. H., et. al., (2008)**, “*World’s Largest (15-inch) XGA AMLCD Panel Using IGZO Oxide TFT*”, in Proceeding SID Digital Technology Papers, pp. 625–628.
17. **Park J. H., et. al., (2011)**, “*Surface-Potential-Based Analytic DC I-V Model with Effective Electron Density for a-IGZO TFTs Considering the Parasitic Resistance*”, IEEE Electron Device Letters, vol. 32, no 11, pp. 1540-1542.
18. **Bae M., et. al., (2011)**, “*Analytical Models for Drain Current and Gate Capacitance in Amorphous InGaZnO Thin-Film Transistors with Effective Carrier Density*”, IEEE Electron Device Letters, vol. 32, no 11, pp. 1546-1548.

19. **Servati P., et. al., (2003)**, “*Above-Threshold Parameter Extraction and Modeling for Amorphous Silicon Thin-Film Transistors*”, IEEE Transaction Electron Devices, Vol. 50, No 11, pp. 2227–2235.
20. **Lee M. J., et. al., (1980)**, “*Electrical and Structural Properties of Cadmium Selenide Thin Film Transistors*”, Solid State Electronics 23, p. 671.
21. **Fung T. C., (2010)**, “*Amorphous In-Ga-Zn-O Thin Film Transistor for Future Optoelectronics*”, a dissertation submitted in partial fulfillment of the requirements for the degree of Doctor of Philosophy (Electrical Engineering) in the University of Michigan, Michigan.
22. **Kanicki J., et. al., (1991)**, “*Performance of Thin Hydro-Genated Amorphous Silicon Thin-Film Transistors*”, Journal of Applied Physics, vol. 69, pp. 2339-2345.
23. **Wu X. D., et. al., (1994)**, “*Imaging with Page Sized a-Si:H 2-Dimensional Sensor Arrays*”, Proceeding SPIE - International Society of Optical Engineering, vol. 2172, pp. 144-154.
24. **Antonuk L. E., et. al., (1998)**, “*A Large-Area, 97 m Pitch, Indirect-Detection, Active Matrix, Flat-Panel Imager (AMFPI)*”, Proceeding SPIE - International Society of Optical Engineering, vol. 3336, pp. 2-13.
25. **Weisfield R. L., et. al., (1998)**, “*New Amorphous-Silicon Image Sensor for x-ray Diagnostic Medical Imaging Applications*”, Proceeding SPIE - International Society of Optical Engineering, vol. 3336, pp. 444-452.
26. **Weisfield R. L., et. al., (1997)**, “*Improved Page-Size 127-m-pixel Amorphous-Silicon Image Sensor for X-ray Diagnostic Medical Imaging Applications*”, Proceeding SPIE - International Society of Optical Engineering, vol. 3032, pp. 14-21.
27. **Karim K. S., Nathan A., (2001)**, “*Readout Circuit in Active Pixel Sensors in Amorphous Silicon Technology*”, IEEE Electron Device Letters, vol. 22, pp. 469-471.

28. **Karim K. S., et. al., (2006)**, “*Amplified Pixel Architectures in Amorphous Silicon Technology for Large Area Digital Imaging Applications*”, Journal of Korean Physics Society, vol. 48, pp. 85-91.
29. **Kamiya T., Hosono H, (2010)**, “*Material Characteristics and Applications of Transparent Amorphous Oxide Semiconductors*”, NPG Asia Materials, pp. 15-22.
30. **Jeong J. K., et. al., (2008)**, “*Distinguished Paper: 12.1-inch WXGA AMOLED Display Driven by Indium-Gallium-Zinc Oxide TFTs Array*”, SID International Symposium Digest Technology Papers, pp. 1-4.
31. **Lee J. H., et. al., (2008)**, “*World's Largest (15-inch) XGA AMLCD Panel Using IGZO Oxide TFT*”, SID International Symposium Digest Technology Papers, pp. 625-628.
32. **Sera K., et. al., (1989)**, “*High-Performance TFTs Fabricated by XeCl Excimer Laser Annealing of Hydrogenated Amorphous-Silicon Film*”, IEEE Transaction Electron Devices, vol. 36, pp. 2868-2872.
33. **Jang J., (2004)**, “*Poly-Si TFTs by Non-Laser Crystallization Methods*”, Thin Film Transistors - Materials and Processes, Vol.2.
34. **Yoon S. Y., et. al., (1998)**, “*Low Temperature Solid Phase Crystallization of Amorphous Silicon at 380C*”, Journal of Applied Physics, vol. 84, pp. 6463-6465.
35. **Jeong J. K., et. al., (2008)**, “*A New Era of Oxide Thin-Film Transistors for Large-Sized AMOLED Displays*”, Information Display, vol. 24, pp. 20-23.
36. **Siddiqui J., et al., (2006)**, “*ZnO Thin-Film Transistors with Polycrystalline (Ba,Sr)TiO₃ Gate Insulators*”, Applied Physics Letters, 212903-1, vol. 88.
37. **Hirao T., et. al., (2006)**, “*Distinguished Paper: High Mobility Top-Gate Zinc Oxide Thin-Film Transistors (ZnO-TFTs) for Active-Matrix Liquid Crystal Displays*”, SID International Symposium Digest Technology Papers, vol. 37, pp. 18-20.

38. **Kim T. H., et. al., (2008)**, “*Electrical Stability of ZnO TFT During Gate-Bias Stress*”, SID International Symposium Digest Technology Papers, vol. 39, 1250-1253.
39. **Hosono H., (2006)**, “*Ionic Amorphous Oxide Semiconductors: Material Design, Carrier Transport, and Device Application*”, Journal of Non-Crystalline Solids, vol. 352, pp. 851-858.
40. **Kamiya T., et. al., (2010)**, “*Present Status of Amorphous In-Ga-Zn-O Thin-Film Transistors*”, Science and Technology of Advanced Materials, 11, 044305.
41. **Hack M., Shur M., Shaw J. G., (1989)**, “*Physical Models for Amorphous Thin-Film Transistors and Their Implementation in a Circuit Simulation Program*”, IEEE Transactions on Electron Devices, 36 (12), 2764.
42. **Colalongo L., (2001)**, “*A New Analytical Model for Amorphous-Silicon Thin-Film Transistors Including Tail and Deep States*”, Solid State Electronics, vol. 45, pp. 1525-1530.
43. **Brews J. R., (1978)**, “*A Charge-Sheet Model of the MOSFET*”, Solid State Electron, 21, 345.
44. **Jeon Y. W., et. al., (2010)**, “*Subgap Density-of-States-Based Amorphous Oxide Thin Film Transistor Simulator (DeAOTS)*”, IEEE Transactions on Electron Devices, vol. 57, no 11, pp. 2988-3000.
45. **Hack M., Shur M., Shaw J. G., (1989)**, “*A New Analytic Model for Amorphous Silicon Thin-Film Transistors*”, Journal of Applied Physics, vol. 66, no. 7, pp. 3371–3380.
46. **Jacunski M. D., Shur M. S., Hack M., (1996)**, “*Threshold Voltage, Field Effect Mobility, and Gate-to-Channel Capacitance in Polysilicon TFTs*”, IEEE Transactions Electron Devices, vol. 43, no. 9, pp. 1433–1440.

47. **Shur M., Hack M., (1984)**, “*Physics of Amorphous Silicon Based Alloy Field-Effect Transistors*”, Journal of Applied Physics, vol. 55, no. 10, pp. 3831–3842.

48. **Chen S. S., Kuo J.B., (1994)**, “*An Analytical a-Si:H TFT DC/Capacitance Model Using an Effective Temperature Approach for Deriving a Switching Time Model for an Inverter Circuit Considering Deep and Tail States*”, IEEE Transactions Electron Devices, vol. 41, no. 7, pp. 1169–1178.

49. **Shur M. S., et. al., (1997)**, “*SPICE Models for Amorphous Silicon and Polysilicon Thin Film Transistors*”, Journal of Electrochemical Society, vol. 144, no. 8, pp. 2833–2839.

50. **Jackson W. B., Hoffman R. L., Herman G. S., (2005)**, “*High-Performance Flexible Zinc tin Oxide Field-Effect Transistors*”, Applied Physics Letters, 193503-1, vol. 87.

51. **Jackson W. B., Hoffman R. L., Herman G. S., (2005)**, “*High-Performance Flexible Zinc Tin Oxide Field-Effect Transistors*”, Applied Physics Letters, 193503-1, vol. 87.

52. **Presley R. E., et. al., (2006)**, “*Transparent Ring Oscillator Based on Indium Gallium Oxide Thin-Film Transistors*”, Solid-State Electronics, 500-3, vol. 50.

53. <http://www.mathworks.com/products/curvefitting/> (Data Download Date: 02.08.2014)

54. **Jeon Y. W., et. al., (2011)**, “*Physics-Based SPICE Model of a-InGaZnO Thin Film Transistor Using Verilog-A*”, Journal of Semiconductor Technology and Science, vol. 11, no. 3.

APPENDICES A

SAMPLE MATLAB CODES

```
%This code is written to sketch the graphs that
%are given in Chapter 2.
clc;
clear all;
close all;

%%% constants

W=225*10^(-6); %m
L=30*10^(-6); %m
Lov=5*10^(-6); %m
Tox=100*10^(-9); %m
%Tigzo=50*10^(-7); %cm
Mband=19.7*10^(-4); %m^2/V.s
Nc=4.8*10^(12); %m^(-3)
Vfb=0.3; %V
Neff1=8.7*10^(11); %m^(-3)
kTeff1=0.045*(1.6*10^(-19)); %eV
Neff2=5.15*10^(11); %m^(-3)
kTeff2=0.0263*(1.6*10^(-19)); %eV
Cox=42.37*10^(-5); %F/m^2
phiF0=0.3; %V
q = 1.6*10^(-19); %e
Eo=8.85*10^(-12); %F/m
eIGZO=11.5*Eo; %F/m
kT=0.026*q;

%%%%%%%%%%%%%%%%%%%%%%%%%%%%%%%%%%%%%%%%%%%%%%%%%%%%%%%%%%%%%%%%%%%%%%%%

syms phis;

Vgs=[3 6 9 12]; %V
Vds=0:0.5:15; %V

C=((2/kT)-(3/(2*kTeff1)));

B=((1/kT)-(1/(2*kTeff1)));

A=(Nc*sqrt(eIGZO))/(B*sqrt(2*Neff1*kTeff1));

for i=1:length(Vgs)
    for j=1:length(Vds)
        phiss(i)=solve(phis-phiF0-2*(kTeff1/q)...
            *log(Cox*(Vgs(i)-Vfb-phis)/sqrt(2*eIGZO*Neff1*kTeff1)));
    end
end
```

```

        phisd(i,j)=solve(phiss-phiss2-2*(kTeff1/q)...
            *log(Cox*(Vgs(i)-Vfb-phiss)/sqrt(2*eIGZO*Neff1*kTeff1)));
    Idssub(i,j)= (W/L)*Mband*(A*Nc)/(2*Neff1*kTeff1*C)...
        *((Cox/sqrt(2*eIGZO*Neff1*kTeff1))^(2*C*kTeff1))*...
        (((2*C*kTeff1+1)^(-1))*((Vgs(i)-Vfb-phiss(i))...
            ^ (2*C*kTeff1+1))-((Vgs(i)-Vfb-phisd(i,j))...
            ^ (2*C*kTeff1+1)))-((q*C)^(-1))*((Vgs(i)-Vfb-phiss(i))...
            ^ (2*C*kTeff1))-((Vgs(i)-Vfb-phisd(i,j))^(2*C*kTeff1)));
    end
end

figure(1)
plot(Vds,Idssub,'-o','LineWidth',1.5);
%set(gca,'FontSize',12);
xlabel('V_D_S (V)','FontSize',12);
ylabel('I_D_Ssub (A)','FontSize',12);
grid on;

C2=((2/kT)-(3/(2*kTeff2)));
B2=((1/kT)-(1/(2*kTeff2)));
A2=(Nc*sqrt(eIGZO))/(B2*sqrt(2*Neff2*kTeff2));

X2=(W/L)*Mband*(A2*Nc)/(2*Neff2*kTeff2*C2);
Y2=((Cox/sqrt(2*eIGZO*Neff2*kTeff2))^(2*C2*kTeff2));

for i=1:length(Vgs)
    for j=1:length(Vds)
        phiss2(i)=solve(phiss-phiss2-2*(kTeff2/q)...
            *log(Cox*(Vgs(i)-Vfb-phiss)/sqrt(2*eIGZO*Neff2*kTeff2)));
        phisd2(i,j)=solve(phiss-phiss2-Vds(j)-2*(kTeff2/q)...
            *log(Cox*(Vgs(i)-Vfb-phiss)/sqrt(2*eIGZO*Neff2*kTeff2)));
        Idsabove(i,j)= (W/L)*Mband*(A2*Nc)/(2*Neff2*kTeff2*C2)...
            *((Cox/sqrt(2*eIGZO*Neff2*kTeff2))^(2*C2*kTeff2))*...
            (((2*C2*kTeff2+1)^(-1))*((Vgs(i)-Vfb-phiss2(i))...
                ^ (2*C2*kTeff2+1))-((Vgs(i)-Vfb-phisd2(i,j))...
                ^ (2*C2*kTeff2+1)))-((q*C2)^(-1))...
            *((Vgs(i)-Vfb-phiss2(i))^(2*C2*kTeff2))...
            -((Vgs(i)-Vfb-phisd2(i,j))^(2*C2*kTeff2)));
    end
end

figure(2)
plot(Vds,Idsabove,'-o','LineWidth',1.5);
%set(gca,'FontSize',12);
xlabel('V_D_S (V)','FontSize',12);
ylabel('I_D_Sabove (A)','FontSize',12);
grid on;

for i=1:length(Vgs)
    for j=1:length(Vds)
        Ids(i,j)=(1/Idssub(i,j))+1/Idsabove(i,j);
        Ids(i,j)=1/Ids(i,j);
    end
end

```

```
        end
    end

    figure(3)
    plot(Vds,Ids,'-o','LineWidth',1.5);
    %set(gca,'FontSize',12);
    xlabel('V_D_S (V)','FontSize',12);
    ylabel('I_D_S total (A)','FontSize',12);
    grid on;

    figure(4)

    surf(Vds,Vgs,double(phisd));

    xlabel('V_D_S');
    ylabel('V_G_S');
    zlabel('phi_S_D');
```

APPENDICES B

CURRICULUM VITAE

PERSONAL INFORMATION

Surname, Name: Bozkurt, İbrahim

Nationality: Turkish (TC)

Date and Place of Birth: 11 November 1988, Adana

Marital Status: Single

Phone: +90 506 710 05 01

e-mail: ibrahimbozkurt@cankaya.edu.tr



EDUCATION

Degree	Institution	Year of Graduation
M.Sc	Çankaya University Electronic and Communication Engineering	January, 2015
B.Sc	Çankaya University Electronic and Communication Engineering	June, 2011
High School	19 Mayıs High School, Mersin	June, 2006

FOREIGN LANGUAGE

Advanced English

PUBLICATION

Bozkurt İ., Çil C. Z., Çalbıyık G., “Lazer ile Mesafe Ölçüm Sistemi”, Çankaya Üniversitesi 5. Mühendislik ve Teknoloji Sempozyumu, Ankara, Türkiye, Apr. 2012. Çankaya Üniversitesi 5. Mühendislik ve Teknoloji Sempozyumu Kitapçığı, 55-60, 26-27 Nisan 2012.

Preveze B., Bozkurt İ., “Bilişsel Ağlarda SNR-Düğüm Yoğunluğu İlişkisi Kullanılarak en iyi Rota Hızı ve en iyi Güç Tüketimi için Optimum Düğüm Yoğunluğunun Saptanması”, Çankaya Üniversitesi 7. Mühendislik ve Teknoloji Sempozyumu, Ankara, Türkiye, May 2014. Çankaya Üniversitesi 7. Mühendislik ve Teknoloji Sempozyumu Kitapçığı, 169-172, 15-16 Mayıs 2014.